Diffusion Tensor Imaging

development and application of a measurement setup to investigate ischemia induced diffusion changes

Jennekens, W.

Award date:
2004

TU/e

MRL

Diffusion Tensor Imaging

Development and application of a measurement setup to investigate ischemia induced diffusion changes

W. Jennekens

April 2004
MRL/KFM 2004-01

ID nr: 465625
Eindhoven University of Technology
Faculty of Applied Physics
Department of Medical Physics

Supervisors:
ir. C. van Pul (TU/e)
Prof.dr.ir. K. Kopinga (TU/e)
Prof.dr.ir. P.F.F. Wijn (TU/e, MMC)

TPM

Abstract

Perinatal hypoxia-ischemia is a major cause of neonatal morbidity and mortality. Diffusion Tensor Imaging (DTI), a Magnetic Resonance Imaging (MRI) technique using diffusion as contrast mechanism, is able to visualize ischemic regions because of their abnormal diffusion. Several theories have been developed to explain these changes in diffusion during ischemia, but none of these are conclusive. An improved understanding of water diffusion and the acute changes that occur after injury may increase the sensitivity and specificity of DTI as a marker of acute brain injury.

In this study, a setup is developed to investigate the mechanisms governing ischemia induced diffusion changes. The rat hippocampus, a well accepted ischemia model, is used as in vitro model tissue and subjected to systematic changes of environment. During these changes, diffusion is monitored using DTI.

Through calibration and validation measurements, the setup was shown to yield realistic values for both diffusion coefficient (*ADC*) and anisotropy (*FA*). Following validations, the hippocampal structure of rat pups (8-12 days old) has been visualized, with resolutions of 141 μm (in vitro) and 62.5 μm (ex vivo)

Without perfusion fluid perturbations, the *ADC* and *FA* of hippocampal slices were shown to remain constant for several hours, and tissue was shown to be viable using a live/dead fluorescence staining.

Cell volume changes, induced by osmotic perturbations, yield clear changes in *ADC*. Decreasing the osmotic value of the perfusion fluid results in a maximum *ADC* decrease of approximately 20%. Anisotropy changes are less pronounced.

Ischemia is simulated through oxygen and glucose deprivation of the perfusion fluid. Both the amount of the *ADC* decrease ($\sim$50%) and the timescale (5-10 h) of the decrease following oxygen and glucose deprivation agree with *ADC* changes observed in clinical studies. The observed decrease can not fully be explained by changes due to cell swelling. The anisotropy shows an increase and subsequent renormalization within several hours. These changes are less evident than the *ADC* changes, and interpretation requires follow-up studies.

Contents

Abbreviations

aCSF	Artificial Cerebrospinal Fluid
ADC	Apparent Diffusion Coefficient
ATP	Adenosine Triphosphate
CBF	Cerebral Blood Flow
CLSM	Confocal Laser Scanning Microscopy
CO	Cardiac Output
CSF	Cerebrospinal Fluid
CT	Computed Tomography
DTI	Diffusion Tensor Imaging
DWI	Diffusion Weighted Imaging
ECS	Extracellular Space
FA	Fractional Anisotropy
FID	Free Induction Decay
FOV	Field Of View
FSE	Fast Spin Echo
FT	Fourier Transform
GM	Gray Matter
HSE	Hahn Spin Echo
ICS	Intracellular Space
LSM	Laser Scanning Microscopy
MRI	Magnetic Resonance Imaging
PFG	Pulsed Field Gradient
RARE	Rapid Acquisition of Repeated Echoes
RF	Radiofrequency
RMS	Root Mean Square
ROI	Region Of Interest
SE	Spin Echo
SNR	Signal to Noise Ratio
SI	Signal Intensity
SS	Slice Selection
TE	Echo Time
TF	Turbo Factor
TR	Repetition Time
TSE	Turbo Spin Echo
WM	White Matter

Symbols

α	Flip angle	deg
γ	Gyromagnetic ratio	Hz/T
δ	Diffusion gradient duration	s
Δ	Diffusion gradient moment	s
ε	Gradient rise time	s
λ	Eigenvalue of the diffusion tensor	m^2/s
ρ	Spin density	AU
ω	Frequency	1/s
ω_0	Larmor frequency	1/s

b	Diffusion weighting	s/m^2
B	Magnetic field	T
B_0	Main magnetic field	T
B_1	RF magnetic field	T
d_{ss}	Imaging slice thickness	m
D	Diffusion constant	m^2/s
FOV	Field of view	m^2
G	Magnetic field gradient	T/m
M	Matrix size	pixels
M_0	Equilibrium magnetization	AU
M_T	Transverse magnetization	AU
M_z	z-component of the magnetization	AU
NSA	Number of Signal Averages	-
t_{90}	Duration of the 90-degree pulse	s
t_{180}	Duration of the 180-degree pulse	s
t_{diff}	Diffusion time	s
T_1	Longitudinal relaxation time	s
T_2	Transversal relaxation time	s
T_2^*	T_2 relaxation time including the effects of field inhomogeneities	s
T_{RF}	RF-pulse duration	s
TE	Echo time	s
TI	Inversion time	s
TR	Repetition time	s

Chapter 1

Introduction

Although there have been major improvements in obstetric and perinatal[1] care, perinatal hypoxia-ischemia[2] or birth asphyxia[3] remains one of the major causes of neonatal morbidity and mortality. The incidence of perinatal asphyxia and of neurological deficits caused by perinatal asphyxia range from 2.0 to 12.0 per 1000 live births and from 0.2 to 2.6 per 1000 live births respectively. Premature infants have a high incidence of perinatal hypoxia-ischemia, i.e. about 600 per 1000 live births. In European countries, the overall mortality due to perinatal asphyxia is 0.85 per 1000 [1].

When hypoxia-ischemia is detected at an early stage, it is thought possible to reverse its effects and prevent or limit permanent injury. The time period in which intervention can be beneficial is referred to as the therapeutic window. For adults, this window lasts until about 3-6 hours from the onset of the insult [2]. For neonates, the therapeutic window is expected to be larger since perinatal hypoxic-ischemic encephalopathy may evolve over several days [3].

Diffusion Weighted Imaging (DWI), a Magnetic Resonance Imaging (MRI) technique using diffusion as contrast mechanism, is able to visualize ischemic regions because of their abnormal diffusion. An example of DWI can be seen in Figure 1.1. Abnormalities are visible in DWI before they can be detected with other imaging modalities (eg. T_1- or T_2-weighted MRI, ultrasound or CT[4]). DWI may therefore be used in the early diagnosis of acute or hyper-acute perinatal hypoxia-ischemia. It might be possible that with DWI changes can be detected while within the therapeutic window, i.e. before there is irreversible damage. Diffusion Tensor Imaging (DTI) is an extension of DWI, measuring diffusion in at least six directions. This technique is sensitive to tissue structure. One of the visualization methods is based on displaying diffusion anisotropy, as shown in Figure 1.1 (*FA*).

Aim of this study

Several theories have been developed to explain the changes in diffusion during ischemia, but none of these are conclusive. An improved understanding of water diffusion and the acute changes that occur after injury may increase the sensitivity and specificity of DWI as a marker of acute brain injury. The goal of this study is to build a measurement setup to investigate the mechanisms governing these changes. The rat hippocampus, a well accepted ischemia model [1, 4], is used as in vitro model tissue. A setup is developed to make DTI measurements of perfused hippocampal slices possible. A slice can be subjected to systematic perturbations of perfusion fluid to simulate ischemia. During these perturbations, diffusion and anisotropy are monitored using Diffusion Tensor Imaging.

[1] The perinatal period is the interval of time between the 28th week of pregnancy and the 8th day after birth

[2] Hypoxia-ischemia is the lack of oxygen and nutrients due to a local decrease in blood flow

[3] Birth asphyxia is fetal suffocation during delivery

[4] Computed Tomography, an X-ray based three-dimensional imaging modality

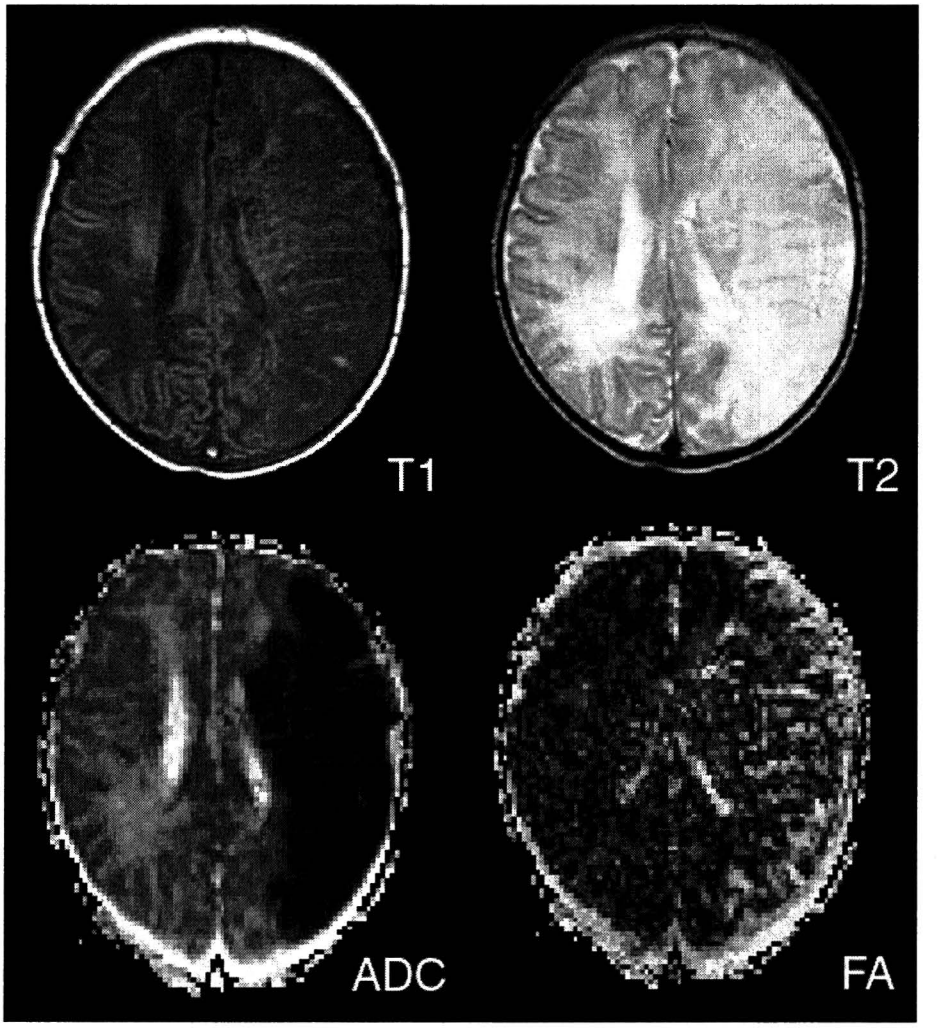

Figure 1.1: MR images of a neonate with a large ischemic brain lesion. Displayed are T_1-weighted (T_1, top left), T_2-weighted (T_2, top right), Apparent Diffusion Coefficient (*ADC*, bottom left) and Fractional Anisotropy (*FA*, bottom right) images. In the *ADC* image, a reduced diffusion in the ischemic region is evident as a dark region. The *FA* image shows an increased anisotropy in this region.

Report outline

In Chapter 2, the MRI basics are briefly summarized, and the specific sequences used in this study are explained in more depth. The physiology of human brain tissue, and ischemia induced changes occurring herein, are outlined in Chapter 3. This chapter also discusses the existing theories explaining changes in diffusion during ischemia and gives an overview of existing in vivo and in vitro models. A brief overview of the rat hippocampus, used as an ischemia model in this study, is also presented. Chapter 4 gives an overview of the experimental setup used in this study, which consists of an MRI system and a perfusion system. The results of calibration and validation measurements are presented and discussed in Chapter 5, along with results of first rat hippocampi measurements. Final conclusions are presented in Chapter 6, and recommendations are given in Chapter 7.

Chapter 2

Magnetic Resonance Imaging

In this chapter a brief overview of Magnetic Resonance Imaging is given. Basic concepts are reviewed in Sections 2.1 through 2.6. The specific pulse sequences implemented and used in this study are described in more detail in Section 2.7.

2.1 Precession

Under influence of an externally applied magnetic field $\vec{B_0}$, nuclear spins will precess with the Larmor frequency ω_0, according to

$$\omega_0 = \gamma|\vec{B_0}|, \tag{2.1}$$

with γ the gyromagnetic ratio. For protons, $\gamma/2\pi$ = 42.56 MHz/T. In an equilibrium situation, spins and corresponding magnetic moments are distributed among all possible orientations according to a Boltzmann distribution. Due to this distribution there is a net magnetization vector $\vec{M_0}$, parallel to $\vec{B_0}$. Its orientation can be influenced by applying magnetic fields.

Dynamics of magnetization $\vec{M}$ in a static magnetic field $\vec{B_0}$ are governed by the Bloch equation

$$\frac{d\vec{M}}{dt} = \gamma\vec{M} \times \vec{B_0} + \frac{1}{T_1}(M_0 - M_z) - \frac{1}{T_2}M_{xy}, \tag{2.2}$$

with T_1 and T_2 the characteristic magnetization relaxation times (discussed in more detail in Section 2.4). From this equation it can be seen that, when $\vec{M}$ and $\vec{B_0}$ are not entirely parallel, there is movement of $\vec{M}$ perpendicular to both $\vec{M}$ and $\vec{B_0}$. This is the previously described magnetically induced precession around $\vec{B_0}$.

Magnetization changes due to RF-pulses are usually evaluated in a rotating frame of reference. This frame rotates around the z-axis with the Larmor frequency (x',y',z' = z). In this rotating frame, magnetization precessing with frequency ω_0 appears to be static. Considering this frame of reference and, for educational purpose, very large relaxation times T_1 and T_2, Equation 2.2 is simplified to

$$\frac{d\vec{M}}{dt} = 0, \tag{2.3}$$

Applying a RF magnetic field $\vec{B_1}$, rotating with ω_0 and perpendicular to $\vec{M}$, gives

$$\frac{d\vec{M}}{dt} = \gamma\vec{M} \times \vec{B_1}. \tag{2.4}$$

Through Equation 2.4, a precession of $\vec{M}$ around $\vec{B_1}$ with frequency $\omega = \gamma|\vec{B_1}|$ is described. If $\vec{B_1}$ is pulsed, the angle of rotation α is then given by

$$\alpha = \gamma B_1 \tau, \tag{2.5}$$

with τ the pulse duration.

2.2 Free Induction Decay

In the 90°-Free Induction Decay (FID) pulse sequence, net magnetization is rotated down into the $x'y'$-plane by a 90°-pulse ($\pi/2$-pulse), as can be seen in Figure 2.1. The net magnetization vector begins to precess about the $+z$-axis. The magnitude of the vector decays with time due to spin dephasing.

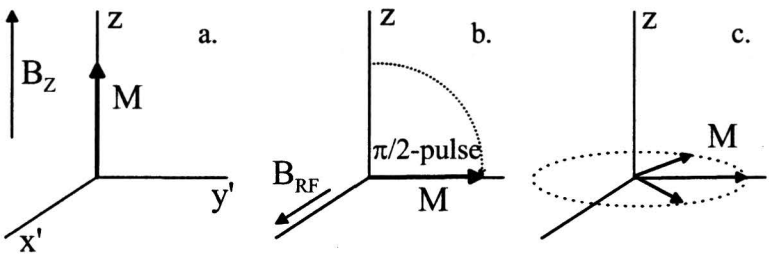

Figure 2.1: Magnetization changes due to a 90°-FID pulse sequence. a) equilibrium situation, magnetization parallel to z-axis. b) $\pi/2$-pulse rotates magnetization into $x'y'$-plane. c) magnetization begins to dephase due to magnetic field inhomogeneities.

2.3 Hahn Spin Echo

Another common pulse sequence is the Hahn Spin-Echo (HSE) pulse sequence, shown in Figure 2.2. Here a 90°-pulse is first applied to the spin system. The 90°-pulse rotates the magnetization down into the $x'y'$-plane. The transverse magnetization begins to dephase, resulting in a FID. At half the echo time (TE) after the 90°-pulse, a 180°-pulse (π-pulse) is applied. This pulse rotates the magnetization by 180° about the x'-axis. This causes the magnetization to rephase and to produce a signal called an echo at the echo time TE. The signal amplitude S is given by

$$S_{TR,TE} = k\rho(1 - e^{-TR/T_1})e^{-TE/T_2}, \tag{2.6}$$

where k is a proportionality constant, ρ is the sample spin density and TR the repetition time, the time between consecutive 90°-pulses. A timing diagram showing RF-pulses and generated signals as function of time can be seen in Figure 2.3.

2.4 Relaxation mechanisms

2.4.1 Spin-Lattice relaxation

Following a RF-pulse, magnetic moments will return to their steady-state orientation, parallel to the z-axis, through interactions with the lattice, the magnetic and nuclear environment of the nucleus. Through these interactions there is dissipation of energy to thermal movement of molecules located in the lattice. In case of a $\pi/2$-pulse, this process is characterized by

$$M_z(t) = M_z(\infty)(1 - e^{-t/T_1}), \tag{2.7}$$

with M_z the z-component of the magnetization, and T_1 the spin-lattice relaxation time.

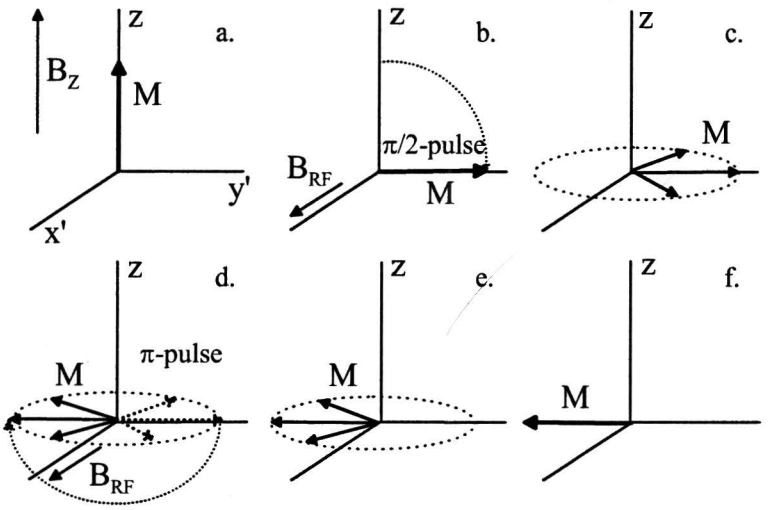

Figure 2.2: Magnetization changes due to a Hahn pulse sequence. a) equilibrium situation, magnetization parallel to z-axis. b) $\pi/2$-pulse rotates magnetization into $x'y'$-plane. c) magnetization begins to dephase due to magnetic field inhomogeneities. d) π-pulse mirrors magnetization in $x'z'$-plane. e) magnetization rephases. f) magnetization in phase: maximum echo signal.

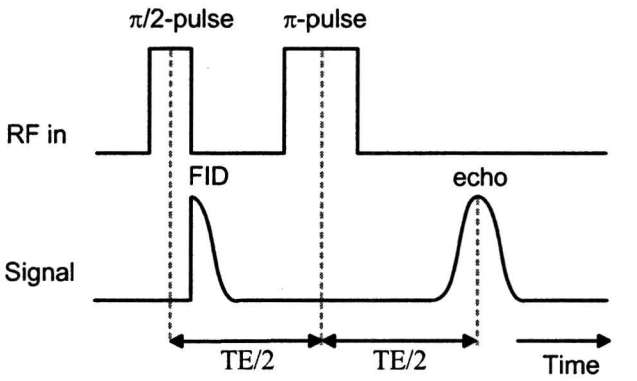

Figure 2.3: Timing diagram for a Hahn pulse sequence, showing the switching of RF pulses and resulting spin-echo signal. 'RF in' is the radio-frequent input signal and 'FID' the Free Induction Decay

2.4.2 Spin-Spin relaxation

Interactions between individual spins cause random fluctuations in local magnetic field, in turn causing fluctuations in precession frequency. Due to these random frequency fluctuations, spins wil gradually lose phase coherence, causing the transverse magnetization M_T to relax back to zero according to

$$M_T(t) = M_T(0)e^{-t/T_2}, \tag{2.8}$$

with T_2 the spin-spin relaxation time.

Due to inhomogeneities of B_0 and the frequency bandwidth of the excitation pulse, spins will be excited at a range of frequencies. This gives rise to an extra loss of phase coherence. The effective

transverse magnetization decay time T_2^* is therefore given by

$$\frac{1}{T_2^*} = \frac{1}{T_2} + \frac{\gamma}{2\pi}\Delta B, \tag{2.9}$$

with ΔB a quantification of macroscopic magnetic field inhomogeneities.

2.5 Spatial encoding

To be able to reconstruct an image, it is necessary to obtain spatial information from the spin-echo signal. This is achieved through slice selection, frequency encoding and phase encoding.

2.5.1 Slice selection

Slice selection is accomplished by applying a linear magnetic field gradient $G_i = dB_z/di$, with i the encoding direction, during the RF-pulses. Due to this gradient, the resonance condition depends linearly on the position. Only spins with a Larmor frequency within the frequency bandwidth of the excitation pulse will be excited. These spins are located within a slice of finite thickness, perpendicular to the direction of the slice selection gradient. By changing the selection gradient, slice thickness can be altered. The slice profile is determined by the shape of the excitation pulse. Sinc-shaped pulses give a uniform slice profile, while hard (block shaped) pulses result in sinc-shaped slice profiles. For a hard pulse, the frequency content is obtained by Fourier transformation and is given by

$$X(\omega) = \frac{2\sin(\omega T_{RF}/2)}{\omega}, \tag{2.10}$$

with T_{RF} the duration of the excitation pulse during the selection gradient (Figure 2.4). A measure for

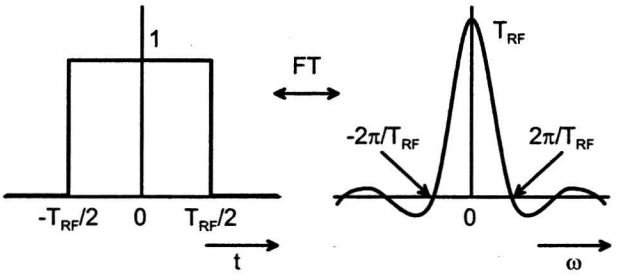

Figure 2.4: Hard RF pulse and its Fourier transform.

the frequency bandwidth of a hard pulse can be given by only considering the main lobe of the sinc function. The width of this lobe is $\Delta\omega = 4\pi/T_{RF}$, or

$$\Delta f = \frac{\Delta\omega}{2\pi} = \frac{2}{T_{RF}}. \tag{2.11}$$

A measure for slice thickness d_{SS} of a hard RF pulse is thus given by

$$d_{SS} = \frac{\Delta f}{\gamma G} = \frac{2}{\gamma G T_{RF}}. \tag{2.12}$$

2.5.2 Frequency encoding

By applying a gradient during signal acquisition, called a read-out gradient, the Larmor frequency depends linearly on the position according to

$$\omega = \gamma(B_0 + iG_j) = \omega_0 + \gamma j G_j, \tag{2.13}$$

with j the encoding direction. Signal intensity and position along the frequency encoding axis can be obtained by analyzing the Fourier spectrum of the signal.

2.5.3 Phase encoding

The phase encoding gradient is used to impart a specific phase angle to a transverse magnetization vector. The gradient is switched on for a short period of time, resulting in a temporary position dependence of the Larmor frequency. After this period, the Larmor frequency will be the same for all spins, but their phase will depend on their position along the phase encoding axis. If a resolution of N points in the phase encoding direction is desired, N different magnitudes of the phase encoding gradient are required.

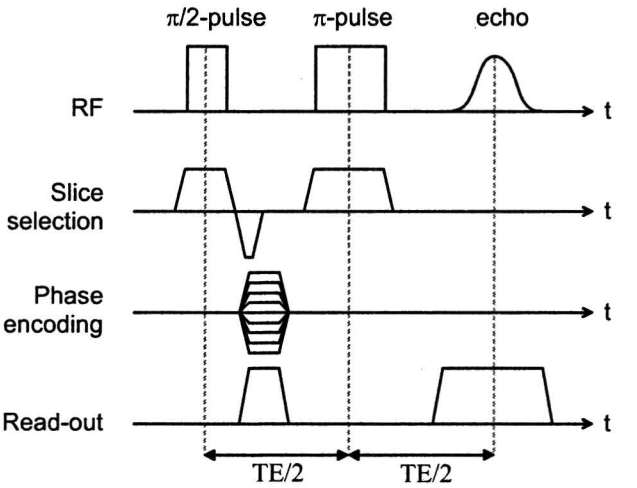

Figure 2.5: Timing diagram for a Hahn spin echo sequence. The switching of RF excitation pulses and spatial encoding gradients is shown as function of time.

2.6 k-space

The distribution of magnetization m over a slice in normal space (x, y) can be expressed as a Fourier transform of the transverse magnetization M_T in k-space (k_x, k_y) according to

$$m(x,y) = \frac{1}{2\pi}\int_{k_x}\int_{k_y} M_T(k_x,k_y)\exp(j(k_x x + k_y y))dk_x dk_y, \tag{2.14}$$

with

$$k_x(t) = \gamma\int_{t_e}^{t} G_x(t')dt', \qquad \text{and} \qquad k_y(t) = \gamma\int_{t_e}^{t} G_y(t')dt', \tag{2.15}$$

where t_e is the timepoint of last excitation and $G_x(t)$ and $G_y(t)$ the time dependent magnetic field gradients in x and y-direction. The velocity along the k-space trajectory at a certain point in time is

$$\frac{dk_x}{dt} = \gamma G_x(t), \qquad \text{and} \qquad \frac{dk_y}{dt} = \gamma G_y(t), \tag{2.16}$$

and its direction is given by

$$\frac{dk_y}{dk_x} = \frac{G_y(t)}{G_x(t)}. \tag{2.17}$$

To be able to reconstruct an image, measurements must be performed in such a way that the complete k-space is filled.

An example of a k-space trajectory can be seen in Figure 2.6, where the trajectory for a part of the Hahn Spin Echo sequence of Figure 2.5 is shown. In this figure, position A is reached by applying

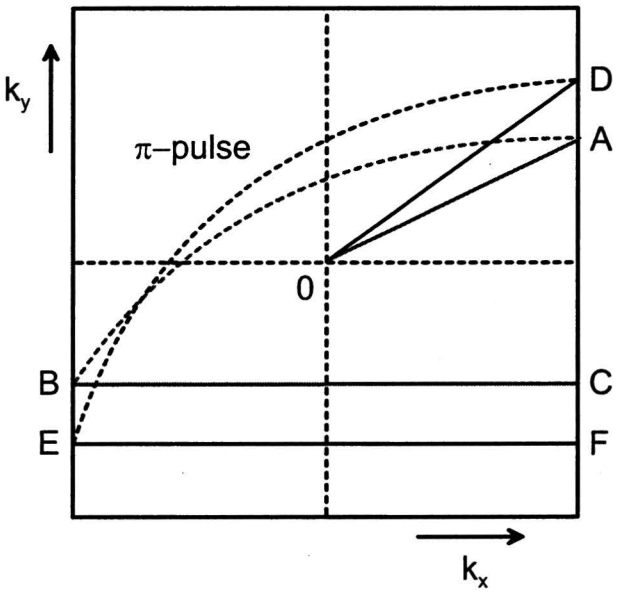

Figure 2.6: k-space trajectory of a Hahn Spin Echo sequence. One spin echo is recorded in the trajectory 0 - A - B - C and, by using a different phase encoding gradient, another is recorded in 0 - D - E - F.

readout and phase encoding gradients. The 180-degree pulse mirrors the position in k-space with respect to the origin, leading to position B. Position C is then reached by once more applying a readout gradient. By using different phase encoding gradients for each step, other trajectories can be followed (e.g. 0 - D - E - F), the complete k-space can be filled and an image can be reconstructed.

2.7 Advanced sequences

The following section describes the specific pulse sequences implemented and used in this study. Specific details are given in Section A.

2.7.1 Diffusion Weighted Imaging

Due to thermal agitation, molecules move and collide. This movement, called diffusion or Brownian motion, results in random molecular displacemens. The mean square displacement $\langle r^2 \rangle$ of Brownian motion is given by

$$\langle r^2 \rangle = 6Dt_{\text{diff}}, \tag{2.18}$$

with D the diffusion coefficient and t_{diff} the diffusion time.

Diffusion can be detected by adding (bipolar) pulsed field gradients (PFG's) to a spin echo sequence [5], as shown in Figure 2.7. The first PFG will result in dephasing of spins, shown in Figure 2.8. In the absence of movement, the second PFG will rephase the spins again, and no net effect is observed.

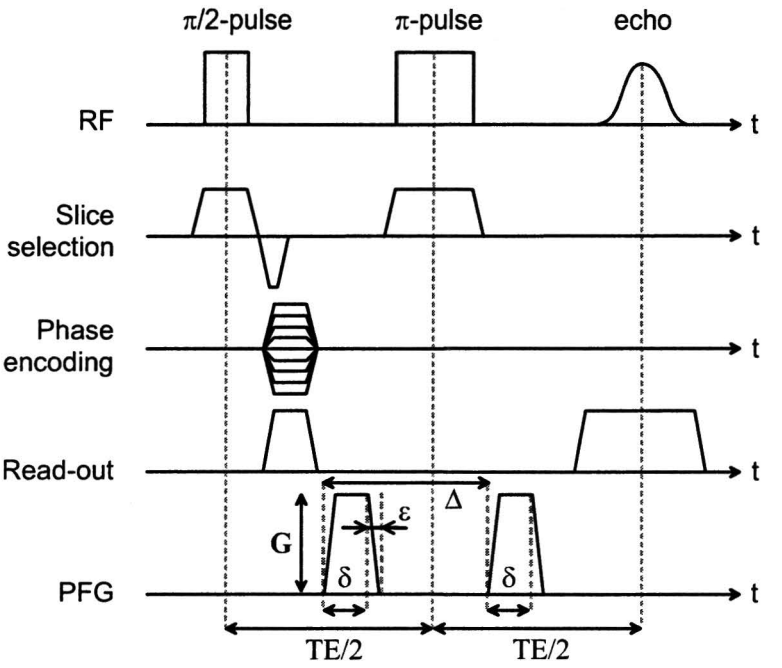

Figure 2.7: Timing diagram for a Pulsed Field Gradient (PFG) Hahn spin echo sequence. The switching of RF excitation pulses, spatial encoding gradients and PFG's is shown as function of time. PFG's are placed symmetrically around the π-pulse, with gradient strength G, gradient duration δ and time between the onset of the first and second gradient Δ.

In case of diffusion however, spins will move during the time interval between the pulses, and will experience a different field during the second PFG. Therefore rephasing will not be exact. Because movement due to diffusion is stochastic, the phase difference of all spins in a voxel combined will also be random, resulting in a net signal loss. The amount of diffusion weighting is expressed in the b-value, defined as

$$b = \int_0^{TE} k^2(t)dt. \tag{2.19}$$

For trapezoidal shaped PFG's, with strength G, duration δ, time between the onset of the first and second gradient Δ and rise time ϵ, as shown in Figure 2.7, the b-value is given by

$$b = \gamma^2 G^2[\delta^2(\Delta - \frac{\delta}{3}) + \frac{\epsilon^3}{30} - \frac{\delta\epsilon^2}{6}]. \tag{2.20}$$

Signal intensity S is then described by

$$S_{TR,TE,b} = k\rho(1 - e^{-TR/T_1})e^{-TE/T_2}e^{-b \cdot ADC}, \tag{2.21}$$

with ADC the Apparent Diffusion Coefficient. The word 'apparent' is included in recognition of the fact that the measurement of diffusion may be influenced by restricted molecular motion caused by cell membranes and other tissue compartments.

The ADC can be determined by eliminating the TR and TE dependence from Equation 2.21. This is done by dividing the signal intensities of images made with and without PFG's for each voxel. This gives

$$\frac{S_b}{S_0} = exp(-b \cdot ADC), \tag{2.22}$$

with S_0 the signal intensity without PFG's, and S_b the signal intensity at a known b-value.

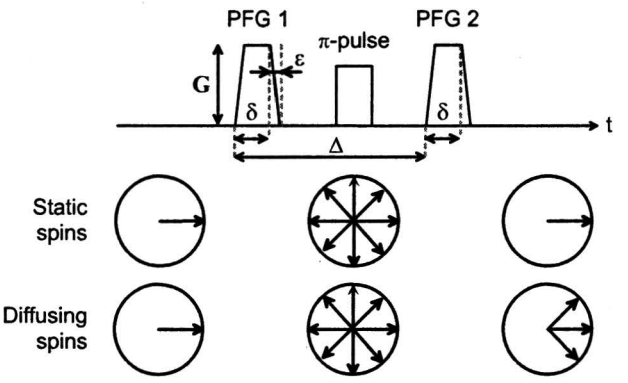

Figure 2.8: Phase shifts in $x'y'$-plane, for static and diffusing spins, due to PFG's.

Diffusion Tensor Imaging

As mentioned, diffusion measurements are sensitive to restricted molecular motion and thus to tissue structure. The directional information can be described by defining a diffusion tensor, according to

$$\underline{\underline{D}} = \begin{pmatrix} D_{xx} & D_{xy} & D_{xz} \\ D_{xy} & D_{yy} & D_{yz} \\ D_{xz} & D_{yz} & D_{zz} \end{pmatrix}, \tag{2.23}$$

with D_{ij} the diffusion coefficient as measured in direction ij. The interpretation of this tensor can be examined by considering a set of identical particles, of which a part is labelled. The flux $\underline{J}$ of labelled particles is then given by

$$\underline{J} = -\underline{\underline{D}} \cdot \nabla \underline{n_a}, \tag{2.24}$$

with $\nabla \underline{n_a}$ the derivative of the labelled particle density. Combining Equations 2.23 and 2.24 gives

$$\begin{pmatrix} J_x \\ J_y \\ J_z \end{pmatrix} = - \begin{pmatrix} \frac{\partial n}{\partial x} D_{xx} + \frac{\partial n}{\partial y} D_{xy} + \frac{\partial n}{\partial z} D_{xz} \\ \frac{\partial n}{\partial x} D_{xy} + \frac{\partial n}{\partial y} D_{yy} + \frac{\partial n}{\partial z} D_{yz} \\ \frac{\partial n}{\partial x} D_{xz} + \frac{\partial n}{\partial y} D_{yz} + \frac{\partial n}{\partial z} D_{zz} \end{pmatrix}, \tag{2.25}$$

from which it is obvious that the off-diagonal elements of 2.23 relate the particle flux in direction i to the derivative of the labelled particles density in direction j. The optimal gradient scheme [6] used to measure the diffusion tensor is given in Table 2.1.

PFG	gradient vector		
	x	y	z
1	1.000	0.000	0.000
2	0.447	0.895	0.000
3	0.447	0.277	0.850
4	0.447	-0.724	-0.525
5	0.447	-0.724	0.525
6	-0.447	-0.277	0.850

Table 2.1: Optimized gradient scheme for Diffusion Tensor Imaging with six gradient vectors [6].

Diffusion anisotropy can be quantified by various anisotropy indices. A commonly used index is the Fractional Anisotropy (*FA*), defined as

$$FA = \frac{1}{2}\sqrt{2} \cdot \sqrt{\frac{(\lambda_1 - \lambda_2)^2 + (\lambda_2 - \lambda_3)^2 + (\lambda_3 - \lambda_1)^2}{\cdot(\lambda_1)^2 + (\lambda_2)^2 + (\lambda_3)^2}}, \tag{2.26}$$

with λ_1, λ_2 and λ_3 the eigenvectors of the diffusion tensor (Eq. 2.23). For an isotropic medium $FA = 0$, while for a cylindrically symmetric anisotropic medium, i.e. $\lambda_1 \gg \lambda_2 \approx \lambda_3 \approx 0$, $FA = 1$.

2.7.2 Turbo Spin Echo

The long scan time characteristic of spin-echo measurements can be reduced by acquiring several profiles per excitation. In a Turbo Spin Echo (TSE) sequence[1], this is accomplished through the addition of multiple refocussing pulses and read-out gradients. Each 180° refocussing pulse inverts the magnetization again, which will rephase in a newly applied read-out gradient, resulting in a new echo. This process is limited only by T_2 decay, decreasing the amplitude of each consecutive echo. The number of consecutive echoes is called the Turbo Factor (TF). Figure 2.9 shows the timing diagram for a TSE sequence. To

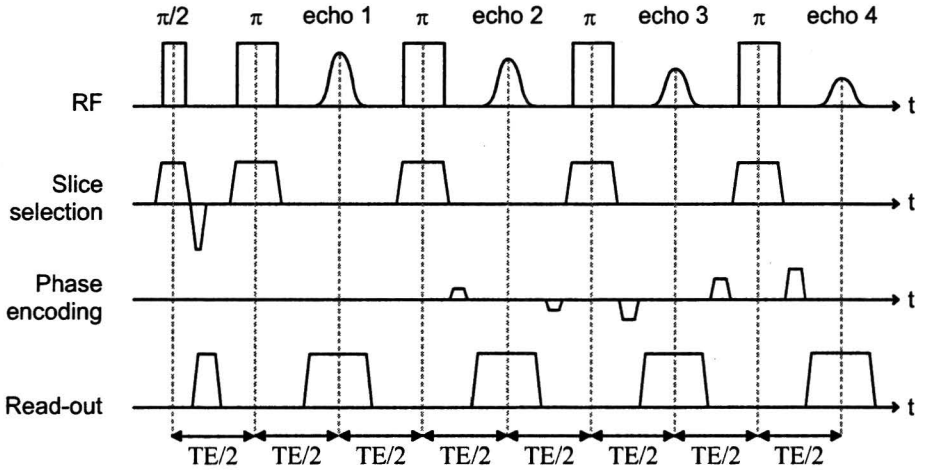

Figure 2.9: Timing diagram for a turbo spin echo (TSE) sequence. The example, at Turbo Factor 4, shows the switching of RF excitation pulses and spatial encoding gradients as function of time. Due to T_2 decay the amplitude of each consecutive echo decreases

minimize the effect of T_2 decay, a "centric" k-line order is used. This line order has the advantage that the k-space center, which determines contrast, has the highest signal intensity. The k-space trajectory of a centric TSE sequence can be seen in Figure 2.10. Because of the periodic signal decrease towards outer k-space lines, some ghosting and blurring can be present in the image [7].

[1] Also known as Fast Spin Echo (FSE) or Rapid Acquisition of Repeated Echoes (RARE)

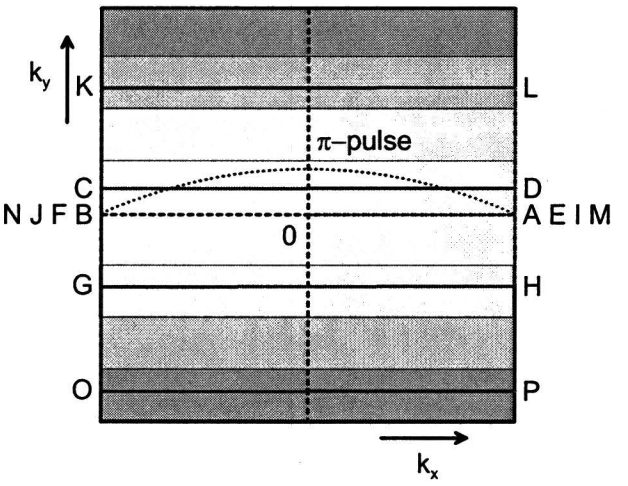

Figure 2.10: k-space trajectory of a Turbo Spin Echo sequence with centric k-line order. In the example, at Turbo Factor 4, the sequence is executed in alphabetical order, 0 - A thru P. Signal intensity is indicated by grayscale value.

Chapter 3

Physiology

In this chapter, an overview of physiology and of physiological phenomena during and after ischemia is presented. Human brain tissue in general is outlined in Section 3.1. The biophysical and DTI changes during ischemia and the existing theories explaining these DTI changes are discussed in Section 3.2. A brief overview of existing ischemia models is given in Section 3.3. The rat hippocampus, chosen as in vitro ischemia model in this study, is discussed in more detail in Section 3.4.

3.1 Human brain tissue

Brain tissue can roughly be divided into white matter (WM) and gray matter (GM). Figure 3.1 shows a cross-section of the human brain. White matter consists of (myelinated) axons and glia cells. Gray

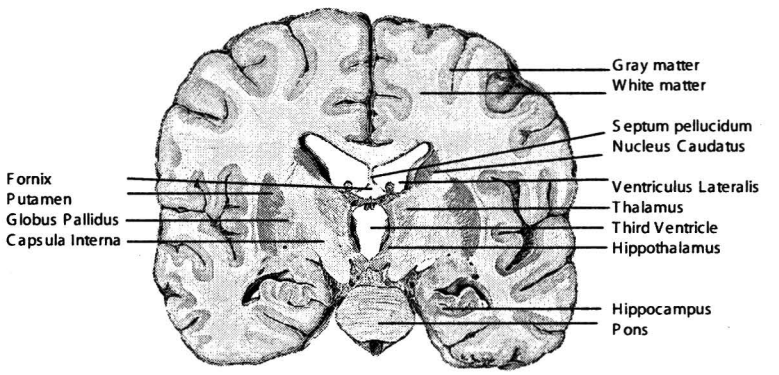

Figure 3.1: Coronal cross-section of the human brain, displaying several important regions, among others white matter, gray matter and the hippocampus.

matter consists of neuron cell bodies and glia cells, as schematically shown in Figure 3.2. All cells are surrounded by the extracellular space, occupying about 20% of the total volume.

The most significant constituent of the brain is the neuron. Neurons consist of dendrites, a cell body and an axon (Figure 3.2). Their function is the transmission of electrical stimuli, known as action potentials. This is achieved through temporary depolarization of the cell membrane by increasing its sodium and potassium permeability. Dendrites are the receptive areas of the neuron. The perikaryon is the neuronal cell body, which contains the nucleus, and its size ranges from 5 to 140 μm. Typical brain axon lengths range from 1 to 10 cm, and diameters from 0.5 to 10 μm. Axons can be surrounded by myelin sheaths, layers of lipids and proteins, increasing the velocity of electrical conduction 5-fold to 50-fold.

Neurons are surrounded by glia cells. These cells are supportive tissue for the brain. They can be

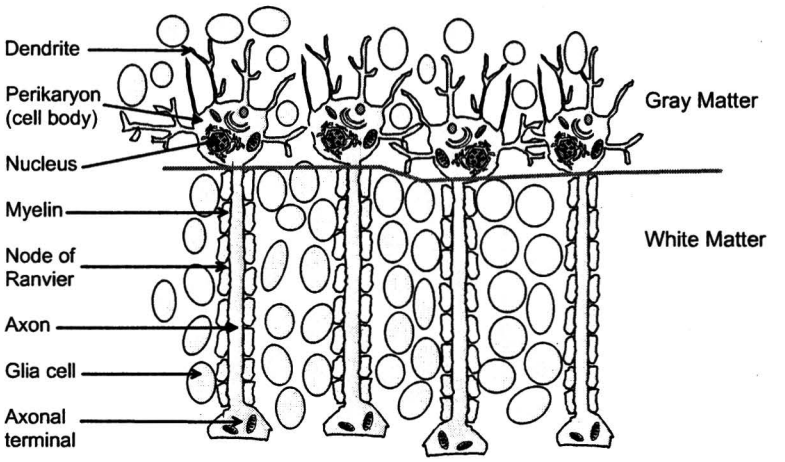

Figure 3.2: Structure of gray matter and white matter. Gray matter comprises neuronal cell bodies and glia cells, while (myelinated) axons surrounded by glia cells constitute the white matter.

subdivided into astrocytes, microglia, ependymal cells and oligodendrocytes. Astrocytes are large cells providing structural support of neurons in the central nervous system. They can absorb glucose from blood and convert it to lactate or glycogen molecules. Astrocytes also help to maintain the appropriate ionic composition of the extracellular fluid. Microglia are the smallest glial cells. Their role is the phagocytosis of necrotic neurons. The myelin sheaths around neurons are produced by oligodendrocytes, the equivalent of Schwann cells in peripheral nervous system. This is achieved by concentrically wrapping multiple layers of oligodendrocyte membrane around one or more axons. Ependymal cells are the epithelial cells lining the neural tube, the ventricles of the brain and the cisterns and subarachnoid space around the brain. All these cavities contain cerebrospinal fluid (CSF).

Cells are provided with oxygen and nutrients through blood, which is transported throughout the whole brain via capillaries, or small blood vessels. From these capillaries, oxygen and nutrients are transported to the cell membrane mainly through diffusion. The cell membrane is active-selective semi-permeable, which means that some molecules can diffuse through the membrane freely, while other molecules have to enter the cell through active transport processes, e.g. through the Na-K pump. For some molecules, the membrane is impermeable. Inside the cell, diffusion is still an important transport mechanism, but in most neurons with their long axons it's effectiveness is limited. Here more active transport processes, like cell streaming, dominate.

3.2 Ischemia

Ischemia is a (local) decrease in blood flow, due to e.g. birth asphyxia, emboly or thrombosis, resulting in hypoxia and lack of nutrients and minerals. The physiological processes resulting from ischemia are complex and not fully understood [8]. Cerebral ischemia can be classified according to its distribution (global vs focal) and duration (permanent vs transient).

Global ischemia is characterized by a widespread, uniform, severe to complete decrease in cerebral blood flow (CBF). Clinically relevant global ischemia is usually temporary (e.g. birth asphyxia or cardiac arrest followed by resuscitation), otherwise it is normally followed by death. Focal ischemia can result from occlusion of a brain artery. In focally ischemic tissue, three regions can be identified: the ischemic core, the penumbra and the periphery. In the ischemic core there is irreversible tissue damage, with non-specific cell necrosis. The penumbra is characterized by reversible tissue damage, and will undergo delayed necrosis after about five hours if no intervention is made. During the ischemic insult, penumbral

tissue is sustained by anaerobic glycolysis. Peripheral tissue will recover within hours after the insult. There is no delayed cell necrosis.

The exact manifestation of ischemia induced damage, and the timing of the mechanisms causing this damage, depend on the type and duration of the ischemia. Ischemia may be either permanent, or transient when followed by reperfusion.

Despite the differences between different types of ischemia, general processes occurring during ischemia can be identified. Because of the lack of oxygen, cells switch to anaerobic glycolysis to maintain adequate levels of ATP. Anaerobic glycolysis leads to the formation of lactate and an increasing acidity of the cells. When glucose is exhausted, ATP depletion will rapidly follow. Due to ATP depletion, ion pumps cease to function and cells are unable to maintain their membrane potential (depolarization). There is an influx of Na^+, Cl^- and Ca^{2+}, and an efflux of K^+. Due to the increased intracellular ion concentration and resulting osmotic pressure difference between the intracellular space (ICS) and the extracellular space (ECS), there is an influx of water, leading to cell swelling or cytotoxic edema.

If the ischemic period is brief, ATP production can be resumed, membranes can be repolarized, and neuronal function may recover. However, reperfusion can trigger or accelerate destructive processes that result in delayed or secondary cerebral damage. There are several proposed mechanisms [9, 8] for this delayed damage, among them the intracellular Ca^{2+} level rise, which could lead to slowed triggering of cell destructing events, protein synthesis depression, which could interfere with maintenance of normal cellular structure and functioning (e.g. inhibition of synthesis of repair proteins), and ischemia induced DNA damage in apoptosis-like cell death, which could lead to late manifestation of cell injury.

If the ischemia persists, the water influx into cells causes the osmotic value of the ECS to increase. Due to the osmotic gradient between the blood compartment and the edemic tissue, there is a net displacement of water from blood to the ECS. The blood brain barrier starts to become more permeable, leading to a displacement of macromolecules to the ECS. Macroscopic swelling, or vasogenic edema, is detectable after five to six hours. This process is characterized by tissue disintegration and the breakdown of the blood brain barrier. Cells become necrotic and are removed through phagocytosis by macrophages.

3.2.1 Ischemia induced DTI changes

The physiological changes described in the preceding section can be monitored using Diffusion Tensor Imaging. The time course of the diffusion coefficient (*ADC*) has been measured in various studies, as reviewed by Sotak [10], however, the time course of the anisotropy (*FA*) has not been extensively studied yet. By observing the time course of both *ADC* and *FA*, different phases of ischemia can be identified, as shown in Figure 3.3. The time course shown in this figure is based upon clinical studies in humans [14, 10]. The time course in animal models is slightly different.

The hyper-acute phase, to six hours after the onset of the ischemic insult, is characterized by a decreased *ADC* accompanied by an increased *FA*. The *ADC* decrease is nonuniform in brain lesions. In the ischemic core the *ADC* will drop to about 50% to 70% of its normal value [14, 10], while the penumbra shows an intermediate reduction. There is very little change in T_2 and tissue water content in this period. The *ADC* decrease provides a unique basis for early visualization of ischemia. In this phase cell membranes and myelin sheaths are still intact.

After about six hours, vasogenic edema starts to develop and T_2-weighted images start to show differences between the ischemic lesion and contralateral tissue. The *ADC* rises above normal after four to six days. The rise in *ADC* is presumably caused by a reduced tortuosity, resulting from the degradation of restrictive barriers due to cell necrosis and accompanying loss of cell membrane integrity. This disruption of cytoarchitecture leads to a loss of anisotropic structures, resulting in a decrease in *FA* in the sub-acute and chronical phase. The chronical phase is generally characterized by a permanently increased *ADC* and decreased *FA*.

Combining *ADC* and *FA*, three phases of diffusion abnormality can be identified: (1) reduced *ADC* and elevated *FA*; (2) reduced *ADC* and reduced *FA*; and (3) elevated *ADC* and reduced *FA*. Although

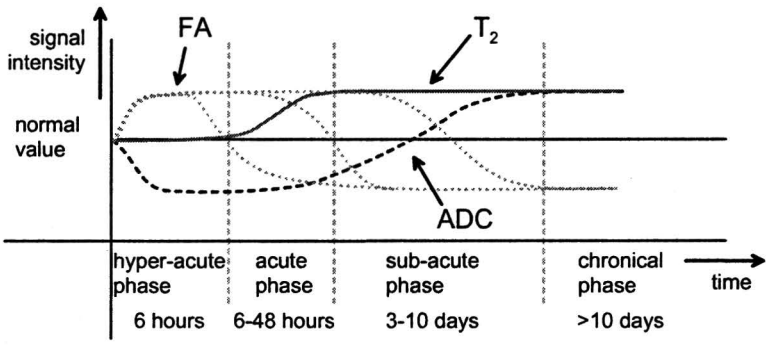

Figure 3.3: Temporal evaluation of *ADC*, *FA* and T_2 in response to ischemia, based upon clinical studies in humans. The course of *FA* can follow three distinct patterns: (1) elevated acutely and subacutely; (2) elevated acutely and reduced subacutely; and (3) reduced acutely and subacutely, as observed by different groups [11, 12, 13]. In the chronical phase, reduced *FA* and elevated *ADC* is generally observed [10].

there clearly are differences in the temporal evaluation of *ADC* and *FA* between subjects, with additional research, (relative differences in) these parameters may prove useful in characterizing the progression of ischemic lesions and may relate to the severity of ischemic insults as well as potential outcomes in response to the initial ischemic injuries [10].

3.2.2 Theories explaining DTI changes

ADC changes

Although the *ADC* decrease accompanying cytotoxic cell swelling is routinely observed, both in clinical and in animal studies, no conclusive theory explaining this change has been formulated. There are several proposed mechanisms that will be discussed:

1. due to cell swelling, there is a reduction in extracellular space. This reduction increases tortuosity in the extracellular compartment, leading to a decreased *ADC*.

2. cell swelling causes a redistribution of water molecules over the intra- and extracellular compartments. Water moves from the fast diffusing compartment (ECS) to the slow diffusing compartment (ICS). The measured *ADC* is a mixed signal of both compartments, thus the increased intracellular water fraction causes the *ADC* to decrease.

3. membrane permeability changes restrict diffusion of water molecules, causing the intrinsic diffusion coefficient to change.

4. reduced intracellular diffusion coefficient, possibly involving early alterations in intracellular tortuosity, cytoplasmic streaming and/or intracellular molecular interactions, causing the *ADC* to decrease.

1. *Tortuosity theory*

The extracellular tortuosity increase theory is supported by studies finding a substantial increase in tortuosity of low molecular weight tracer molecules during progressive ischemia [15] and after total circulatory arrest [16]. Monte Carlo simulations also provide evidence that variations in extracellular diffusion coefficient have a significant impact on tissue *ADC* [17]. The tortuosity theory is contradicted by a study determining extracellular tortuosity after osmotic perturbations in the turtle cerebellum. This study

shows tortuosity changes to be relatively small, and therefore not sufficient to explain the *ADC* decrease accompanying cytotoxic cell swelling [18].

2. *Redistribution theory*

The redistribution theory assumes the intracellular diffusion coefficient to be lower than the extracellular diffusion coefficient. This assumption is corroborated by the fact that the ICS is a crowded environment containing many restricting structures. The redistribution theory is contradicted by a ^{19}F NMR study monitoring 2FDG-6P diffusion in the rat brain, showing no statistical difference between intra- and extracellular *ADC* values in normal or in globally ischemic brain [19]. This study shows that the water *ADC* decreases in both spaces after ischemia, with the reduction of intracellular water motion being the primary source of diffusion-weighted contrast. The assumption that different compartments (ICS, ECS) contribute with a different *ADC* to the signal decay, and that there is no exchange between these compartments, is the basis for studies using high b-values (up to 10000 s/mm^2) to determine the relative fractions of ADC_{fast} and ADC_{slow}. These are found to be 0.8 and 0.2 respectively [20]. If, as hypothesized, the extracellular diffusion coefficient is higher, this is in contradiction with the fact that the extracellular space occupies about 20% of the total volume. Possible explanations for these discrepancies could be water exchange between ICS and ECS during the diffusion time, or T_2 differences between ICS and ECS [20]. Further complications concerning this theory arise from DWI studies of the Xenopus Oocyte. Here evidence is presented that the intracellular space contains both fast and slow water *ADC* components [21].

3. *Permeability theory*

The membrane water permeability change theory assumes nearly free water diffusion across the cell membrane in healthy cerebral tissue due to its relatively high water permeability, which decreases subsequent to the infarct induction, thus resulting in restricted diffusion. Monte Carlo simulations of water diffusion in a simple model of gray matter have contradicted this theory by demonstrating the *ADC* to be relatively insensitive to permeability changes [17].

4. *Intracellular diffusion coefficient theory*

The study of intracellular metabolite *ADC*'s following ischemia [16, 9] has shown that these *ADC*'s are significantly reduced, like the *ADC* of water. This is an indication that changes occur in the ICS. Possible mechanisms for a reduced intracellular diffusion coefficient are reduced cytoplasmic streaming or changes in intracellular viscosity. Cytoplasmic streaming might diminish due to a lack of ATP, while intracellular viscosity changes might result from the breakdown of larger macromolecules, local pH changes leading to protein conformation changes [22] or alterations in the configuration of the cytoplasmic matrix, affecting intracellular tortuosity and molecular interactions [9]. The notion of *ADC* reductions due to changes in cytoplasmic streaming is contradicted by a study of intracellular *ADC* values of small molecules and ions in the Xenopus oocyte. These diffusion coefficients are shown to be primarily size-dependent, indicating that intracellular water motion in the oocyte is mainly Brownian displacement with little or no role for cytoplasmic streaming [23].

Anisotropy changes

Changes in diffusion anisotropy have been observed in a small number of studies [11, 12, 13]. The time points of these changes are controversial, and no extensive research focussed on finding explanations for anisotropy changes has been conducted. The acute diffusion anisotropy increase following ischemia is thought to arise from cell swelling during cytotoxic edema. This swelling would, for white matter, reduce the inter-fiber spacing. The increased extracellular tortuosity may cause increased restriction of

water movement perpendicular to the fiber orientation, and thus increase in anisotropy. The sub-acute and chronic anisotropy decrease is generally attributed to a loss of structural integrity due to membrane degradation and cell lysis [10].

It is clear that additional research is needed to resolve the mechanisms governing changes in diffusion coefficients and diffusion anisotropy following cerebral ischemia. Although cell swelling and increased tortuosity of the ECS seem to play a major role, it is plausible that these changes are brought about by a combination of aforementioned mechanisms [9].

3.3 Ischemia models

Ischemia has been studied extensively using animal models [8, 24]. Ischemia models can be divided into in vivo[1] and in vitro[2] models. While in vivo models are often realistic human representations and therefore complex systems, in vitro models generally offer the benefit of relative simplicity and because of this facilitate interpretation of measurements.

In vivo models

Laboratory rats are the most widely used animals for in vivo experimental cerebral ischemia studies because they are relatively inexpensive, genetically homogeneous and their cerebral circulation shows good homology to that of humans [8, 24]. Larger animals, such as the pig, have also been used to study ischemia. These models are substantially more expensive, but are often better representations of the human cerebral organization and because of this they may be valuable in the final stage of research on therapeutic interventions [1]. Only recently, the availability of transgenic mice has put forward the mouse as ischemia model. Transgenic mice enable studies into the relevance of specific gene products for ischemic injury [24]. In vivo models are used to study ischemic processes, and have resulted in a far better understanding of these processes, however influencing the cellular environment directly, conform in vitro models, is not possible.

In vitro models

In vitro models can de divided into cell culture models and tissue slice models. In cell culture models, ischemia induced damage is easily studied but cell interactions differ significantly from in vivo tissue. An important distinction is the absence of anisotropy. Important tissue slice models are peripheral nerves, the spinal cord and the hippocampus [8]. Peripheral nerves, like the sciatic nerve, are often used in DTI studies, but are not considered ischemia models. The spinal cord is a well accepted ischemia model, but its structure differs significantly from brain tissue. Both peripheral nerves and the spinal cord suffer structure loss when slices are made. Because neuron cell membranes are damaged, cell volume changes due to osmotic perturbations are unclear, as is neuron viability.

The hippocampus is a well known cerebral ischemia model. It is one of the brain areas that is most severely damaged during perinatal hypoxia-ischemia [1]. The diffusion properties of the rat hippocampus are comparable to those of the human hippocampus [4]. It also responds to osmotic perturbations in a fashion similar to that observed in human hippocampal slices. Furthermore, its axons are mostly located in a transverse plane and because of this there is little structure loss when transverse slices are made. Although the hippocampus has often been studied, and tissue perfusion is well documented [25], it has only been studied with MR by one group at the University of Florida [26, 27, 28, 29].

[1] in vivo: within a living organism

[2] in vitro: in an artificial environment, in isolation from a living organism

Because the clinical background of this study concerns perinatal hypoxia-ischemia, the hippocampus of rats pups (8-12 days old) was chosen as in vitro cerebral ischemia model. Because these animals are approximately at the same developmental phase as neonates, they provide a better neonatal ischemia model compared to mature rats. The disadvantage of using immature animals is the smaller hippocampal volume and, due to a lesser degree of myelinization, the lower anisotropy. The advantage of using rat pups is that hippocampal slice viability is easier to maintain [25].

3.4 Rat hippocampus

The rat hippocampal formation appears grossly as an elongated structure with its long axis extending in a C-shaped fashion, as shown in Figure 3.4. The long axis of the hippocampus is referred to as the

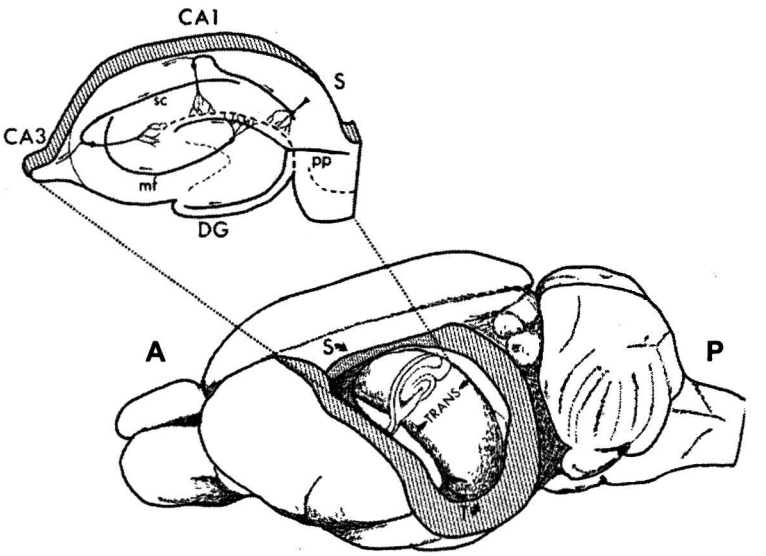

Figure 3.4: Diagram showing the location of the hippocampal formation in the rat brain.

septotemporal axis, while the orthogonal axis is referred to as the transverse axis [30].

The hippocampal formation (Figure 3.5) comprises the dentate gyrus, the hippocampus and the subiculum. The hippocampus is subdivided into the CA1, CA2 and CA3 regions. Following hypoxia-ischemia, damage will be predominantly located in the CA1 region [1]. The hippocampus has numerous connections with the cerebral cortex, as well as with other structures (e.g. the amygdala and the hypothalamus). Its major output pathway is the fornix [31]. The alveus, the thin white band of fibres covering the ventricular surface of the hippocampus, is expected to yield the highest diffusion anisotropy due to its highly ordered structure.

The hippocampus is a critical neuronal decision-making mechanism, determining the type and importance of incoming sensory signals and providing the drive that causes translation of short-term memory into long-term memory. If a neuronal signal is determined to be important, it is likely to be committed to memory. Children born preterm have significantly smaller hippocampal volumes and, due to this, exhibit increased incidence of learning difficulties [32]. Bilateral removal of the hippocampi, sporadically performed as treatment of epilepsy in human beings, causes anterograde amnesia[3] and some retrograde amnesia[4]. Consolidation of long-term memory of the verbal and symbolic type does not take place without hippocampi [31].

[3]Anterograde amnesia: lack of the ability to establish long-term memories lasting longer than a few minutes

[4]Retrograde amnesia: deficits in previously learned memories

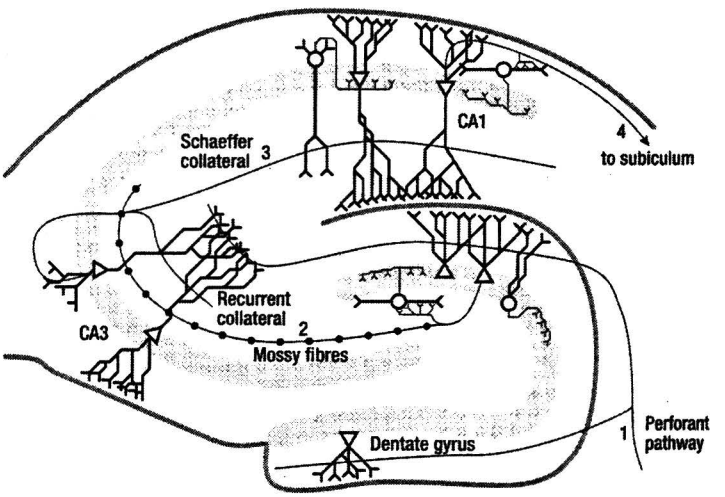

Figure 3.5: Diagram showing regions and fiber orientations in a transverse slice of the rat hippocampus.

Chapter 4

Experimental setup and methods

This chapter describes the experimental setup as used in this study. Sections 4.1 through 4.3 discuss the MRI setup, tissue perfusion and sample preparation. Calibration and validation measurements are described in Section 4.4, which also describes the first applications of the measurement setup.

4.1 MRI system

The main magnetic field $\vec{B}_0$ is generated by a 4.7 T Oxford Instruments magnet, shown in Figure 4.1, a superconducting coil in which a current of 103.7 A is continuously running [33]. The coil is kept at superconducting temperature via a liquid helium bath (4.2 K), which is surrounded by a liquid nitrogen bath (77 K) to prevent the helium from evaporating too quickly.

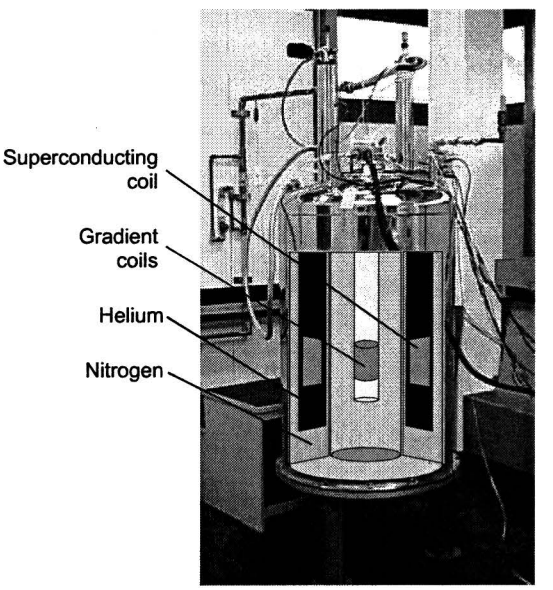

Figure 4.1: Oxford Instruments 4.7 T superconducting magnet with Doty micro imaging insert. Schematic overview of internal components

Magnetic field gradients are generated by a Doty micro imaging insert [34], consisting of x-, y- and z-gradient coils, able to deliver maximum gradients of 800 to 1000 mT/m. The coils have a 4% gradient uniformity (RMS) over a cilinder with a diameter of 32 mm and a length of 32 mm, and are shielded to minimize eddy currents. Gradient rise times are controlled through a gradient control box, developed in this study. This control box also features gradient offset adjustment for each gradient channel, enabling first order shimming of the main magnetic field.

To accomplish radio-frequent excitation and signal detection, a send and receive coil, as shown in Figure 4.2(a), was developed. This coil is a balanced solenoid consisting of three turns, with a diameter

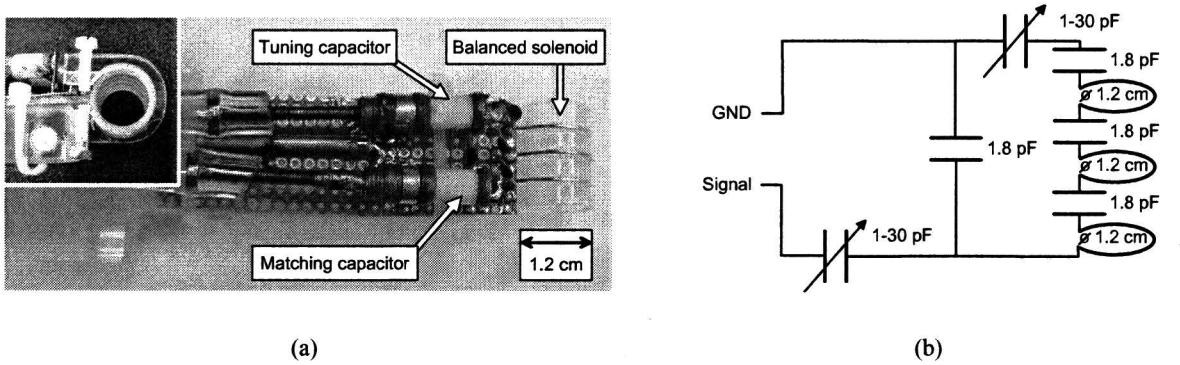

(a) (b)

Figure 4.2: RF-insert (a) with balanced solenoid used for radio-frequent excitation and signal detection, sample holder and tuning and matching capacitors. Sample rotation mechanism is shown in the top left corner. Figure (b) shows an electrical diagram of the coil.

of 12 mm and a mutual separation of 5 mm. An electrical diagram of the coil is shown in Figure 4.2(b), and the frequency characteristics are shown in Figure B.1 of Appendix B.

4.2 Tissue perfusion

To maintain cell viability, hippocampal slices are to be provided with oxygen and nutrients. To accomplish this, a perfusion system was developed to provide tissue slices with artificial cerebrospinal fluid (aCSF) containing O_2, glucose and nutrients, among other substances.

4.2.1 Perfusion system

The perfusion system consists of a basin with bubbling system, a peristaltic pump, an overflow and a perfusion chamber. A schematic diagram of the system can be seen in Figure 4.3(a). The basin contains aCSF, which is saturated with oxygen through the bubbling system. From the basin, saturated aCSF is transported to the overflow via the peristaltic pump, the overflow providing a constant pressure. The flow is measured and controlled by a rotameter with an adjustable valve. From the rotameter, the aCSF is then directed to the perfusion chamber and subsequently back to the basin. The perfusion chamber, shown in Figure 4.3(b), is located inside the magnet. Inside the perfusion chamber, hippocampal slices are placed on a nylon mesh, with a pore diameter of 200 μm. To prevent sample movement, slices are fixed by means of a spacer, with a thickness of 300 μm, a second nylon mesh and a rubber band (not shown).

4.2.2 Artificial cerebrospinal fluid

The composition of the artificial cerebrospinal fluid used to perfuse the hippocampal slices is given in Table 4.1 [28, 25]. The fluid is saturated with Carbogen gas, consisting of 95% O_2 and 5% CO_2, and contains three buffers (HCO_3^-, PO_4^{3-} and SO_4^{2-}), resulting in a pH $\approx$ 7.4. Precise pH adjustment is accomplished by using KOH and HCL solutions.

To simulate ischemia, glucose and oxygen can be omitted from the aCSF. In literature this is known as glucose oxygen deprivation [1, 8]. The osmotic value can be altered by using different quantities of water, for fixed amounts of additives. When osmotic perturbations are made, concentrations are checked

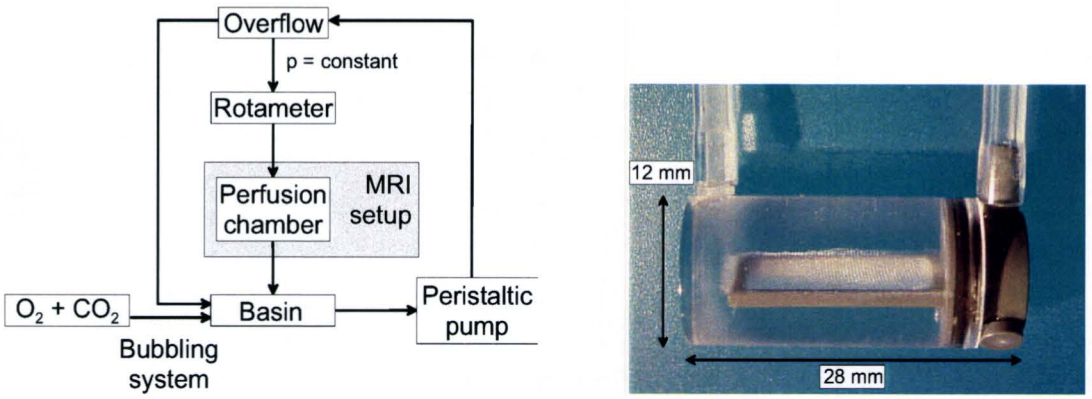

(a) (b)

Figure 4.3: Perfusion system used to supply hippocampal slices with artificial cerebrospinal fluid containing oxygen and nutrients. A schematic diagram of the system is shown in (a), and the perfusion chamber used to fix the sample positions is shown in (b).

Element	Concentration
NaCl	120 mM
KCl	3 mM
Glucose	10 mM
$NaHCO_3$	26 mM
$CaCl_2$	2 mM
KH_2PO_4	1.5 mM
$MgSO_4$	1.4 mM

Table 4.1: Composition of the aCSF used to perfuse hippocampal slices [28, 25].

using ion chromatography (Dionex ICS90, Dionex Corporation, Sunnyvale CA USA, using an IonPac CS12A-5μm separation column and 11 mM H_2SO_4 eluent).

4.3 Sample preparation and viability determination

The slice procurement and viability staining protocols used in this study are based on protocols used in Utrecht [1].

4.3.1 Slice procurement

Rat pups, eight to twelve days old, are sacrificed by decapitation and hippocampal slices are obtained according to the protocol used in Utrecht [1]. Following decapitation, scalp and cranium are opened, the optic nerves are cut and the brain is rapidly removed and placed into aCSF. Brain hemispheres are separated and the hippocampus is extracted from the brain. Using a McIlwain tissue chopper, the hippocampus is cut into 500 μm slices, transverse to the septo-temperal axis. Four to six slices are then selected by means of visual inspection (microscopy), placed on the nylon mesh, secured and placed inside the perfusion chamber. The perfusion chamber is placed in the perfusion setup, taking care to avoid air bubbles inside the chamber, and then positioned inside the magnet.

4.3.2 Viability staining

To verify slice viability following MR measurements, Calcein-AM and Propidium Iodide staining is performed [1, 35]. Stimulation and detection of these fluorescent dyes is accomplished through a Zeiss LSM 510 Confocal Laser Scanning Microscope, equipped with HeNe (633 nm, 5 mW) and Ar (488 nm, 15 mW) lasers.

Calcein-AM

Calcein-AM (Sigma 04558) is employed to mark viable cells. It passes intact cell membranes and, in these live cells, the nonfluorescent calcein-AM is converted to green-fluorescent calcein, after acetoxymethyl ester hydrolysis by intracellular esterases. The absorption maximum of calcein lies at 494 nm and its emission maximum at 517 nm.

Propidium Iodide

Propidium Iodide (PI, Sigma P4864) is a fluorescent stain for nucleic acids of necrotic cells. It binds to DNA, hereby enhancing its fluorescence 20 to 30-fold. PI is membrane impermeant and excluded from viable cells. The absorption maximum of bound PI lies at 535 nm and the emission maximum at 617 nm.

Staining protocol

After completion of MR measurements, viability staining is performed according to a modified protocol [35], based on the protocol used in Utrecht [1]. The hippocampal slices are first transferred from the perfusion chamber to a bin containing 1 ml aCSF. Subsequently, 5 μl Calcein-AM and 1 μl Propidium Iodide are added. These dyes are incubated for thirty minutes at room temperature, while protected from exposure to light. After incubation, slices are rinsed with aCSF for fifteen minutes. CLSM images are then acquired in z-stacks, using magnifications of 2.5x, 10x and 20x. An example of a staining image is shown in Figure 4.4 [35].

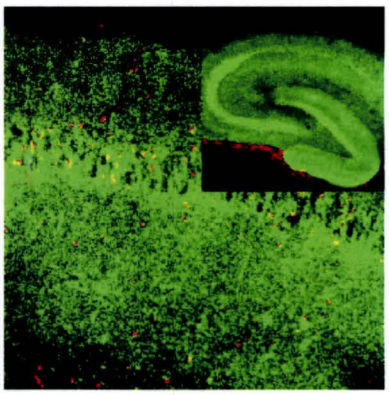

Figure 4.4: CLSM image at magnifications of 5x (inset) and 20x (main) of an oxygen-glucose deprived hippocampal slice, using a live(green)/dead(red) fluorescence assay [35].

4.4 Methods

Because part of the MRI setup and part of the pulse sequences are newly implemented, it is necessary to perform calibration and validation measurements. These measurements are described in Section 4.4.1. Following calibration and verification, measurements on rat hippocampal slices are performed to investigate ischemia induced diffusion changes. These measurements are described in Section 4.4.2.

4.4.1 Calibration measurements

Gradient calibration

For imaging, it is important that the actual magnetic field gradients exactly match input gradients, to prevent image distortion. For DWI measurements this is even more important, as the signal attenuation, and thus the measured diffusion coefficient, depends on the gradient strength (Eq. 2.22).

Gradient strengths are calibrated by imaging a sample of exactly known dimensions, shown in Figure 4.5. This sample is filled with glycerol, which, due to its high viscosity, allows rotation of the sample

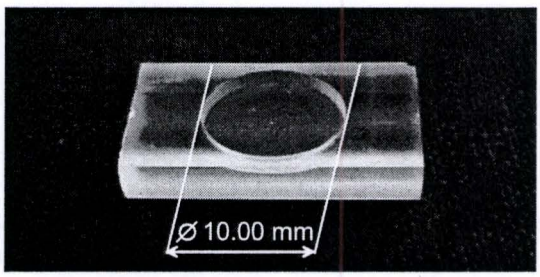

Figure 4.5: Sample constructed for geometric gradient strength calibration.

to the vertical plane without loss of contents. By determining the difference between the calculated and the measured sample widths for the xy- and yz-plane, gradients are scaled to match the settings. Image width is determined by using an edge detection algorithm in combination with an ellipse fit algorithm, yielding a high accuracy. The expected image size d_{im}, in pixels, can be calculated from the sample diameter d_s, the matrix size M and the FOV according to

$$d_{im} = d_s \frac{M}{\sqrt{\text{FOV}}}. \tag{4.1}$$

with $\sqrt{\text{FOV}} = \text{BW}/\gamma G$ it follows that

$$d_{im} = d_s \frac{M\gamma G}{\text{BW}}, \tag{4.2}$$

with BW the receiver bandwidth. From this equation it can be seen that image size is linear with gradient strength. An overestimation of the gradients will result in images being too small, while an underestimation produces images being too large. To prevent blurring of the image, which reduces calibration accuracy, a regular high resolution HSE sequence is used instead of a TSE sequence.

Slice selection rephasing optimization

When slice selection gradients are applied during the 90°-pulse, a rephasing lobe is required to reverse effects of dephasing during slice selection. Inadequate rephasing leads to nett magnetization loss. To minimize signal loss, slice selection rephasing is optimized by varying the length of the rephasing lobe through the use of a scaling factor, while monitoring signal intensity. This is accomplished by using a HSE sequence, while only recording the zeroth k-line for every rephasing lobe length. Because the

k-space center (k_x, k_y) = (0,0) gives the spatial integral over signal intensity, the zeroth k-line gives a measure of overall signal intensity.

Slice profile

Because 'hard' excitation pulses are used, the slice profile will be sinc-shaped, in accordance with Figure 2.4. To quantify the signal contribution of the sinc side-lobes, the exact slice profile is determined. By choosing the slice selection gradient direction to coincide with one of the imaging gradient directions, the slice profile can be visualized. To minimize sample related signal variations, a large homogeneous sample is used.

Echo shift testing

When using a TSE sequence, exact timing is necessary to minimize echo shift induced ghosting. Timing is tested by imaging a sample without using phase encoding gradients. The lack of phase encoding results in the same echo being continually recorded. In k-space, consecutive echoes are then visualized and echo shifts can be identified.

Sample alignment

As the sample position with respect to the magnet coordinate system can only be adjusted by adjusting the height of the sample, it is important for the samples to be located exactly in the slice selection plane. This is accomplished by adjusting sample rotation using a rotation mechanism developed in this study, as shown in Figure 4.2(a), to ensure the sample is located exactly in the horizontal plane.

PFG balancing

Diffusion weighted imaging is conducted using two PFG's, as described in Section 2.7.1. It is important that these gradients are balanced, because unbalanced gradients result in additional dephasing and thus in additional loss of nett magnetization. This loss can erroneously be interpreted as loss due to diffusion, and result in incorrect *ADC* measurements.

Balancing is performed by conducting diffusion weighted measurements on a natural rubber sample, in which (virtually) no signal attenuation due to diffusion is expected. The sequence used for this calibration is a Pulsed Field Gradient HSE. To eliminate image gradient related disturbances, measurements are performed without imaging gradients. By scaling the strength of the second (or rephasing) gradient, echo intensity is maximized and gradient mismatch is minimized for (x, y, z)-directions.

ADC validation

Final gradient verification is achieved by quantitative *ADC* measurements. The *ADC* of a water sample at a known temperature is measured for all PFG directions of Table 2.1 and compared with literature values.

Anisotropy validation

To validate diffusion tensor measurements and subsequent anisotropy calculations, it is first determined wether above mentioned *ADC* validation yields isotropic diffusion. Secondly, diffusion tensor imaging is performed on a porcine optic nerve, which was stored in a freezer for a prolonged period. The optic nerve is known to be anisotropic, with its main diffusion direction parallel to the nerve orientation. Previous DTI measurements on this sample, executed on a 6.3 T scanner immediately following excision, yielded an average diffusion coefficient of $ADC = (0.30 \pm 0.01) \times 10^{-9}$ m^2/s and an average anisotropy

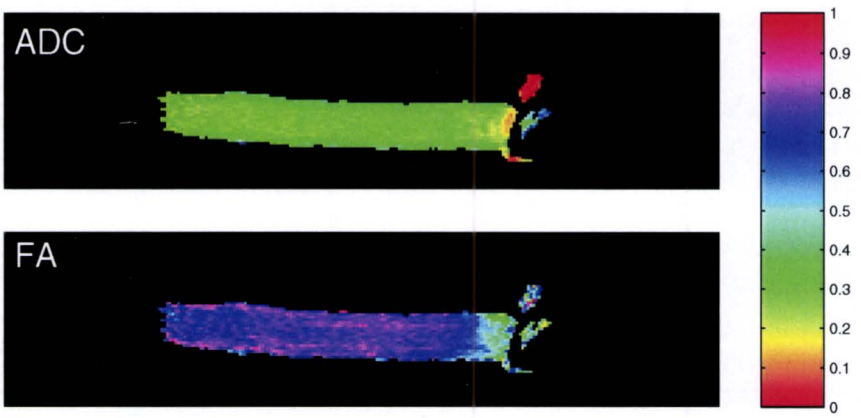

Figure 4.6: *ADC* and *FA* maps of freshly excised porcine optic nerve, as measured on a 6.3 T scanner. The *ADC* is given in units of 10^{-9} m^2/s.

of $FA = (0.76 \pm 0.03)$ for the center region of the optic nerve as shown in Figure 4.6. The average axon diameter is expected to be comparable to the bovine optic nerve axon diameter, estimated to be about (2.6 ± 0.2) μm [36]. From this diameter, above mentioned *ADC* and Equation 2.18, it follows that the diffusion time, which is the time required for water molecules to have probes restricting structures, is in the order of $t_{diff} = 3.8$ ms.

High resolution feasibility

To show the feasibility of imaging rat hippocampi and visualizing contrast between gray matter and white matter, as schematically indicated in Figure 3.5, the hippocampus of an adult rat, fixated using formaldehyde, is imaged.

4.4.2 Hippocampus measurements

As mentioned in Section 3.2.2, several theories have been introduced to explain ischemia induced diffusion changes. To determine the importance of these proposed mechanisms, their individual effects on diffusion can be monitored. The effect of cell volume changes is investigated by means of osmotic perturbations. These effects are compared with the effect of simulated ischemia by means of O_2 and glucose deprivation.

DTI settings

Diffusion Tensor measurements are performed using the sequence settings shown in Table 4.2 in combination with the gradient scheme of Table 2.1 [6]. All DTI measurements are performed for both positive

Parameter	Setting
M	128x64
FOV	20x10 mm^2
TR	3 s
TE	13 ms
NSA	2
TF	4
G_{encode}	200 mT/m
G_{PFG}	600 mT/m
δ	3 ms
Δ	8 ms
b	1628 s/mm^2

Table 4.2: DTI TSE settings for in vitro measurements.

and negative gradient directions, hereby reducing gradient bias effects and doubling NSA. With these settings, acquiring a diffusion tensor takes 45 minutes. Slice selection gradients are chosen to yield an effective slice thickness of approximately 450 μm. The effective slice thickness is defined as the FWHM of the main lobe of the profile shown in Figure 2.4. Signal amplifier gains are optimized for diffusion weighted images as well as for the reference image, necessitating scaling of the reference image.

Continuity measurement

To establish effects of aCSF perturbations on diffusion, it is first necessary to monitor wether the diffusion remains constant without perturbations. To accomplish this, diffusion tensor images are acquired for hippocampal slices perfused with (isotone) oxygen saturated aCSF for a prolonged period. The aCSF flow rate is approximately 5-10 ml/min. To avoid flow artifacts, perfusion is discontinued during diffusion measurements. It has been shown that periodic discontinuation of aCSF flow, up to 35 minutes, does not affect slice viability for at least 8 hours after slice procurement [28]. To establish the time required to prevent residual flow inside the perfusion chamber from influencing the measurement, the *ADC* is first monitored through DWI measurements for a single PFG direction, with Turbo Factor TF = 8, immediately following flow discontinuation. For the DTI measurements pulse sequence settings are given in Table 4.2, and are used in combination with the gradient scheme of Table 2.1.

Osmolarity changes

To determine the effects of cell volume changes on water diffusion, DTI measurements are performed for various aCSF osmolarities. Hypotone aCSF induces cell swelling, while hypertone aCSF induces

cell shrinkage. Slices are first perfused with isotone aCSF and, during flow discontinuation, a baseline diffusion tensor is acquired. Subsequently, slices are perfused with relative aCSF osmolarities between 120% (20% hypertone) and 70% (30% hypotone). During perfusion with a new osmolarity, the *ADC* is monitored through DWI measurements for a single PFG direction, with TF = 8. When the *ADC* stabilizes, a new diffusion tensor is acquired. The pulse sequence settings for the DTI measurements are given in Table 4.2, and are used in combination with the gradient scheme of Table 2.1.

Simulated ischemia

Ischemia is simulated by perfusing hippocampal slices with glucose and O_2 deprived aCSF. Because the timescale of ischemia induced diffusion changes is not exactly known, it is unknown whether DTI measurements give sufficient time resolution to be able to monitor these changes. This necessitates first establishing the actual timescale. Hereto, slices are first perfused with normal oxygen saturated aCSF and, during flow discontinuation, a baseline diffusion tensor is acquired. Subsequently, slices are perfused with glucose and O_2 deprived aCSF, while continuously monitoring the *ADC* through DWI measurements for a single PFG direction, with TF = 8. After 30 minutes, flow is discontinued and the *ADC* is continuously monitored in order to estimate the timescale of diffusion changes. When this timescale is shown to be sufficiently long to allow DTI measurements, subsequent measurements are conducted according to the settings of Tables 4.2 and 2.1.

Complete hippocampus

As mentioned in Section 3.3, most fibers within the hippocampus are located in the transverse plane, and there is little structure loss when transverse slices are made. To visualize the structure of the hippocampus and the presence of longitudinal components of fibers, a diffusion tensor of a complete hippocampus of a rat pup is acquired. This measurement is performed for both a non-fixated hippocampus (ex vivo) and a fixated hippocampus. Immediately after extraction, the hippocampi are frozen or formaldehyde fixated, respectively. The fixation allows for longer measurements without tissue degradation, thus obtaining higher signal-to-noise ratios. The *ADC* of ex vivo and fixated tissue differs, however, it has been shown that fixated tissue retains its anisotropy [37]. Sequence settings are given in Table 4.3, and are used in combination with the gradient scheme of Table 2.1. The Δ = 10 ms for the ex vivo hippocampus is

Parameter	Setting
M	128x128
FOV	8x8 mm^2
TR	3 s
TE	13.5 ms
NSA	22
TF	4
G_{encode}	200 mT/m
G_{PFG}	600 mT/m
δ	3 ms
Δ	10 & 8 ms
b	2092 & 1628 s/mm^2

Table 4.3: DTI TSE settings for measurements of non-fixated and fixated complete hippocampi.

chosen to obtain optimal image contrast. These setting yield an in-plane resolution of 62.5x62.5 μm. Slice thickness according to Eq. 2.12 is set to approximately 1 mm. With these settings, the full tensor take approximately eight hours to acquire.

Chapter 5

Results and discussion

In this chapter, the main results of the research are presented and discussed. As the focus of this graduation research was on the development of a setup to measure DTI changes during ischemia in an experimental model, the first part of this chapter is focused on calibration measurement results and specifications of the setup. In the second part of the chapter, the first results of measurements in rats are presented.

5.1 Calibration and validation results

Before conducting diffusion measurements on hippocampal slices, it is first necessary to perform calibration and validation measurements. The outcomes of these measurements are presented in Sections 5.1.1 through 5.1.9.

5.1.1 Gradient calibration

The gradient strength is calibrated as discussed in Section 4.4.1, using the glycerol filled gradient calibration sample. The results of edge detection and an ellipse fit algorithm, applied to an image of the sample positioned in the xy-plane, after re-adjustment of the gradients, are shown in Figure 5.1. The ellipse fit

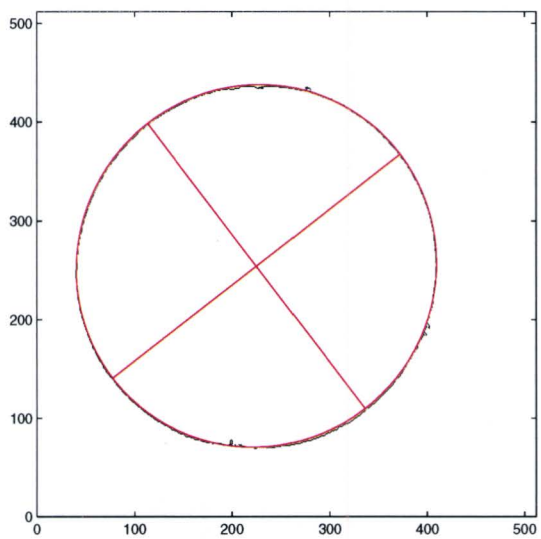

Figure 5.1: Edge detection (black) and ellipse fit (red) of image of glycerol filled geometric gradient calibration sample placed in the xy-plane. HSE settings are 512x512 matrix, FOV = 14 mm, NSA = 16, TR = 0.5 s, TE = 6.5 ms and 300 mT/m imaging gradients.

algorithm yields a long axis of 372 pixels, a short axis of 365 pixels and a rotation of -37.6 degrees. From Equation 4.1 it follows that, with d_s = 10 mm, FOV = 14 mm and M = 512, the correct image size d_{im} is 366 pixels. The fit results are within 2% of the expected value.

Applied to an image of the sample positioned in the yz-plane, the ellipse fit algorithm yields a long axis of 368 pixels, a short axis of 364 pixels and a rotation of 9.2 degrees. These values are within 1% of the expected value of 366 pixels.

5.1.2 Slice selection rephasing optimization

The rephasing length of the slice selection gradient can be adjusted to obtain an optimal SNR. A typical rephasing optimization measurement is displayed in Figure 5.2. For varying rephasing lobe lengths,

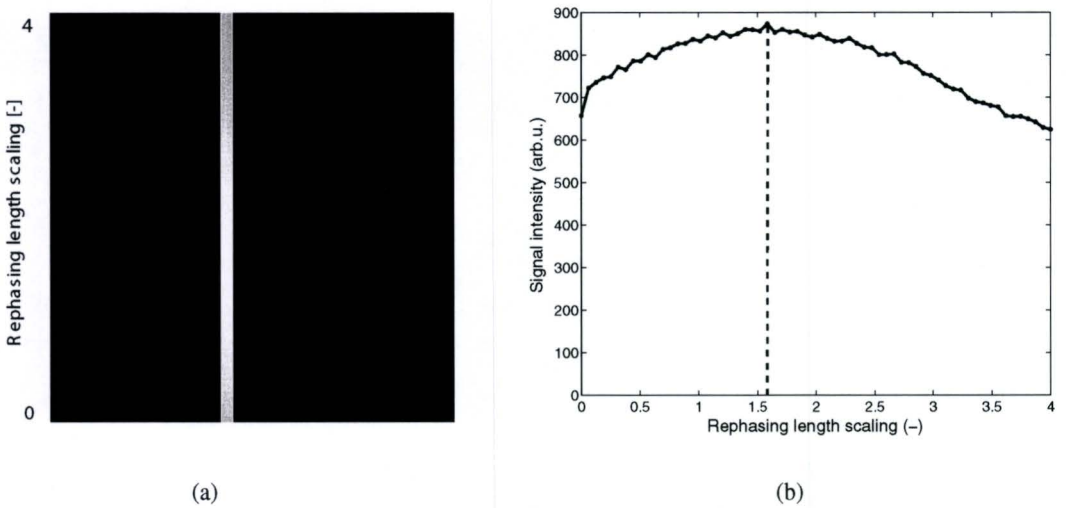

(a) (b)

Figure 5.2: Example of rephasing optimization. Figure (a) shows k-space, with echoes for various rephasing lengths, and Figure (b) shows the intensity profile for echo centers, with a scaling factor of 1.6, indicated by the dashed line, yielding maximum intensity.

echoes are consecutively recorded in k-space (Figure 5.2(a)). From this image, the optimal scaling factor, yielding maximum rephasing and thus maximum signal intensity, can be found through an intensity profile. This profile is obtained by plotting signal intensity for echo centers as function of rephasing length scaling factor (Figure 5.2(b)). In this example, maximum signal intensity is obtained using a scaling factor of 1.6, as indicated by the dashed line.

The optimal scaling factor depends on the exact gradient shape and area, and thus on gradient strength and gradient offsets. Since each measurement is conducted using different gradient strengths and offsets (due to shimming), this optimization is performed before each measurement.

5.1.3 Slice profile

Because 'hard' excitation pulses are used, the slice profile will be sinc-shaped. To characterize the exact shape, and quantify the signal contribution of side-lobes, the slice profile is determined as described in Section 4.4.1, from an image with HSE settings of 128x128 matrix, FOV = 12 mm, NSA = 8, TR = 0.1 s, TE = 2 ms, G_{encode} = 200 mT/m and G_{ss} = 200 mT/m. The slice profile obtained from this measurement is shown in Figure 5.3. In this figure, the sinc-shaped intensity profile can clearly be seen. Full width at full maximum of the main lobe is 16 pixels. The two dashed lines indicate the calculated slice thickness

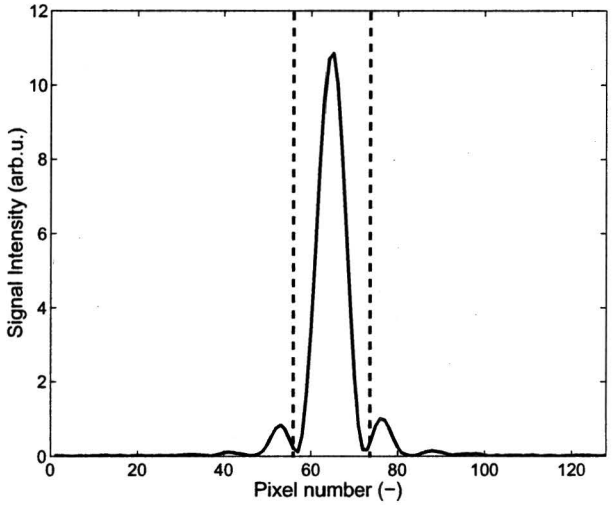

Figure 5.3: Slice profile resulting from block-shaped excitation pulse. Dashed lines indicate the calculated slice thickness according to Eq. 2.12 for the specific RF-pulse duration and gradient strength.

of 17.9 pixels, according to Eq. 2.12 with τ_{180} = 140 μs and G_{ss} = 200 mT/m. The measured slice thickness deviated 10.6% from the calculated thickness.

By determining the total area and the area of the side lobes, it is concluded that the side-lobes contribute approximately 11% to the overall signal intensity.

5.1.4 Echo shift testing

Sequence timing, important to minimize artifacts, is tested by plotting consecutive echoes in k-space, as described in Section 4.4.1. Figure 5.4 shows a typical timing measurement. From this figure, it can be seen that echoes are all placed on a vertical line, indicating correct timing. Furthermore, discrete intensity steps towards outer k-space lines are visible. These steps are due to T_2 decay of the signal, decreasing the intensity of each consecutive echo, as discussed in Section 2.7.2.

5.1.5 Sample alignment

To align the sample plane to the slice selection plane, sample rotation is optimized. The result of this alignment is shown in Figure 5.5. In this figure, the white line indicates an exactly horizontal position. Sample width is measured to be 116 pixels, and at a rotational accuracy of one pixel, it follows that rotation of the sample is accurately in the horizontal plane to within 0.02 rad.

5.1.6 PFG balancing

To minimize excessive dephasing, which results in signal loss and incorrect *ADC* measurements, PFG's require balancing. PGF's are balanced by using a rubber sample and scaling the strength of the rephasing gradient. Echo intensity was maximized and gradient mismatch was eliminated for (x, y, z)-directions. The obtained correction factors, shown in Table 5.1 were validated for gradient strengths throughout the operating range (G_{max} = 650 mT/m).

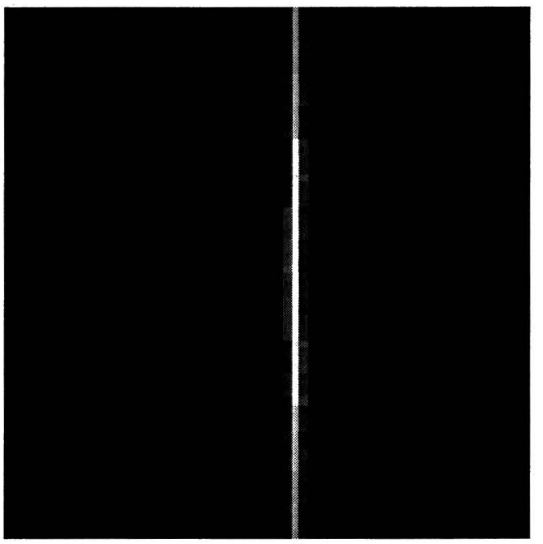

Figure 5.4: Example of echo shift testing, showing k-space with recorded echoes. Image acquired for 64 echoes, with Turbo Factor TF = 4.

PFG	Scaling factor
x	0.99957
y	0.99967
z	0.99955

Table 5.1: PFG scaling factors.

5.1.7 Gradient hardware

Intensive use of high gradients (within specifications) resulted in repeated detaching of gradient connector leads from the print (Figure 5.6). This problem is due to constantly switching Lorentz forces introducing large mechanical strains, and was overcome by replacing the original leads by twisted leads to minimize Lorentz forces and replacing the original print by movable connections to minimize mechanical strains.

5.1.8 ADC validation

To validate *ADC* measurements, quantitative *ADC* measurements were performed for the gradient directions of Table 2.1. Figure 5.7 shows the results of measuring water signal attenuation in a Region Of Interest (ROI), drawn within the sample, as function of diffusion weighting at a water temperature of approximately $21.3°C$. Diffusion weighting is accomplished using the gradient vectors of Table 2.1. Error bars in Figure 5.7 are calculated through

$$\delta\left[\ln\left(\frac{S_b}{S_0}\right)\right] = \sqrt{\left(\frac{1}{S_b}\right)^2 \delta[S_b]^2 + \left(\frac{1}{S_0}\right)^2 \delta[S_0]^2}, \tag{5.1}$$

with S_b and S_0 the average signal in the diffusion weighted image and in the reference image respectively, and σ the standard deviation. The *ADC* is calculated by applying a fitting routing to the data points of Figure 5.7 and determining the derivative of the fit function. In accordance with Eq. 2.22, a linear fit is applied. This fit is not forced through the origin, because the reference image is measured only

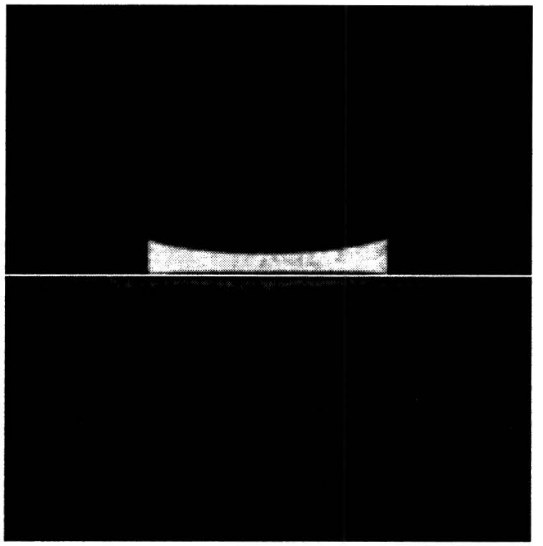

Figure 5.5: Image of glycerol filled sample holder. TSE settings are 256^2 matrix, FOV = 14 mm, NSA = 1, TR = 0.2 s, TE = 5 ms, TF = 4 and 200 mT/m imaging gradients. Slice thickness according to Eq. 2.12 is set to 520 μm. White line indicates the horizontal plane.

once, possibly leading to attenuation calculation offsets. The resulting *ADC*'s are shown in Table 5.2. The average *ADC* is $(2.05 \pm 0.03) \times 10^{-9}$ m^2/s. Literature values for the water diffusion coefficient are shown in Figure C.1 of Appendix C [38, 39], which displays the diffusion coefficient as function of the temperature. Using linear interpolation between the data points of this figure, it can be seen that for a water temperature of $21.3°C$ the diffusion coefficient is 2.106×10^{-9} m^2/s [39] or 1.923×10^{-9} m^2/s [38]. The average measured *ADC* is within the bandwidth between both these literature values, with deviations from these values of +3% and -6% respectively.

5.1.9 Anisotropy validation

The *ADC* measurements of Section 5.1.8 yield a difference of up to 4% between water *ADC*'s for the PFG directions of Table 2.1. This difference results in a maximum *FA* of 0.02 for isotropic structures.

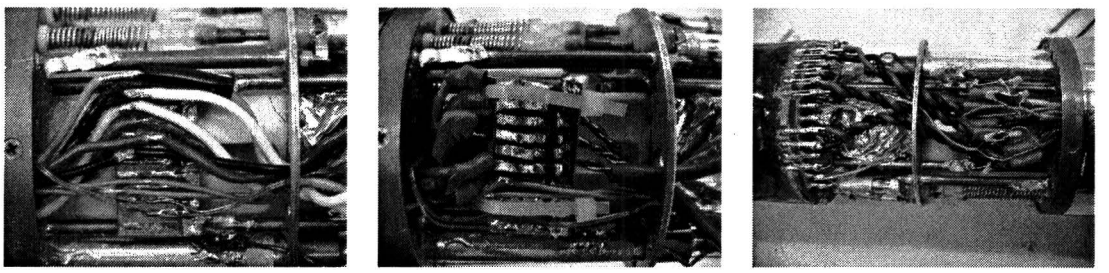

Figure 5.6: Imaging insert gradient connector leads. Left picture displays the original configuration, with leads detached from print due to constantly switching Lorentz forces. Center picture displays the first modification, which proved insufficient to prevent lead failures. Right picture displays current configuration, with twisted wires to minimize Lorentz forces.

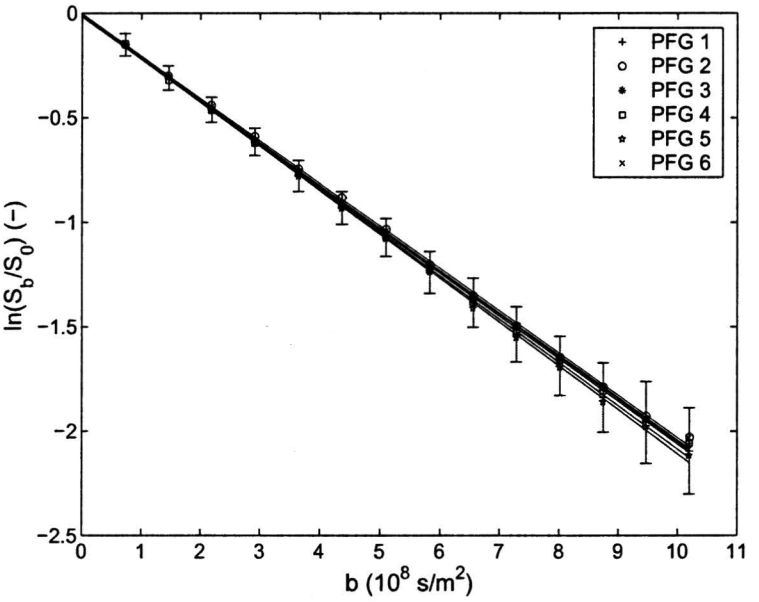

Figure 5.7: Signal attenuation as function of b-value, with a linear fit, for a water filled sample using the PFG directions of Table 2.1 averaged over positive and negative gradients. Water temperature is approximately 21.3°C. To improve clarity, only error bars of PFG 1 are plotted. Fit results are shown in Table 5.2.

PFG	ADC $\pm$ σADC (m^2/s)
1	$(2.07 \pm 0.01)\times10^{-9}$
2	$(2.03 \pm 0.01)\times10^{-9}$
3	$(2.04 \pm 0.01)\times10^{-9}$
4	$(2.04 \pm 0.01)\times10^{-9}$
5	$(2.10 \pm 0.01)\times10^{-9}$
6	$(2.03 \pm 0.01)\times10^{-9}$

Table 5.2: Calculated *ADC* for six gradient vectors [6].

To further validate anisotropy measurements, the *ADC* and *FA* of a porcine optic nerve are measured in a ROI in the upper part of the nerve, as structure is best preserved in this region, and compared to values as measured on a 6.3 T scanner directly following excision. Figure 5.8 displays the measured Apparent Diffusion Coefficient, Fractional Anisotropy and Color Code maps. These images are acquired using a diffusion weighting of b = 1.33×10^9 s/m^2, with a diffusion time Δ = 16 ms. Since the diffusion time in the nerve is estimated to be in the order of t_{diff} = 3.8 ms, as described in Section 4.4.1, Δ = 16 ms is more than sufficient for water molecules to have probed all cellular restrictions, and thus correct anisotropy maps are obtained. The average *ADC* is found to be $(0.53 \pm 0.07)\times10^{-9}$ m^2/s, while an average *FA* of (0.39 ± 0.06) is measured. Compared to the values as measured on a 6.3 T scanner directly following excision (Figure 4.6), the average *ADC* is increased by 77%, while an *FA* decrease of 49% is observed.

By displaying the main diffusion direction for each pixel, the fiber orientation can be visualized. This results in a Color Code map of the optic nerve, as shown in Figure 5.8. From this figure it is clear that the main fiber orientation is parallel to the long axis of the optic nerve, the anterior-posterior direction, as indicated by the green color. The lower section, where the nerve is cut, shows a fiber orientation perpendicular to the long axis, in the right-left direction as indicated by the red color.

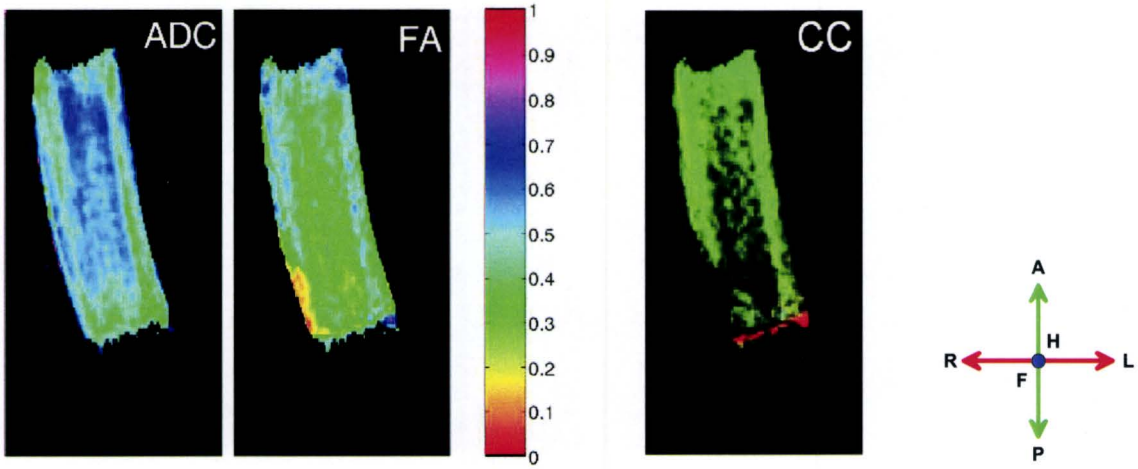

Figure 5.8: *ADC* (left), *FA* (center) and Color Code (right) maps of an excised porcine optic nerve. The *ADC* is given in units of 10^{-9} m^2/s. Color Code map displays the main diffusion directions. Green indicates anterior-posterior, red indicates left-right and blue indicates the out of plane main diffusion direction. Images are acquired using TSE settings of M = 128x128, FOV = 20 mm, NSA = 10, TR = 3 s, TE = 20 ms, TF = 4, G_{encode} = 200 mT/m and G_{ss} = 200 mT/m, yielding an in-plane resolution of 156x156 μm^2 at a slice thickness of approximately 700 μm. PFG setting are G = 550 mT/m, δ = 2 ms and Δ = 16 ms, resulting in a diffusion weighting of b = 1.33×10^9 s/m^2.

5.1.10 High resolution feasibility

To determine the feasibility of imaging a hippocampus and visualizing contrast between gray and white matter, a fixated hippocampus of an adult rat was imaged, as shown in Figure 5.9. This figure displays a diffusion weighted image and an *ADC* image. In these images, the difference between gray matter and white matter, as schematically indicated in Figure 3.5, is clearly visible.

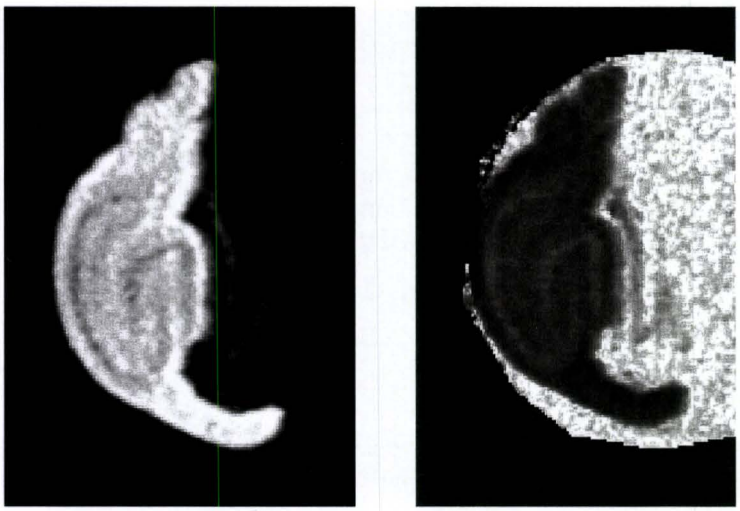

Figure 5.9: DWI (left) and *ADC* (right) images of a fixated complete hippocampus of an adult rat, acquired using TSE settings of M = 256x256, FOV = 12 mm, NSA = 18, TR = 2 s, TE = 16 ms, TF = 4, G_{encode} = 200 mT/m and G_{ss} = 500 mT/m, yielding an in-plane resolution of 47x47 μm^2 at an effective slice thickness of approximately 450 μm. PFG setting are G = 600 mT/m, δ = 3.1 ms and Δ = 6.6 ms, resulting in a diffusion weighting of b = 1.382×10^9 s/m^2.

5.2 Calibration and validation discussion

Calibration and characterization measurements were performed as described, resulting in an optimized SNR and imaging sequence. Subsequent validation measurements yield realistic values for both *ADC* and *FA*.

Maximum *ADC* errors are found to be between +3% and -6% with respect to literature values, shown in Figure C.1 of Appendix C [38, 39]. Although the average measured *ADC* is within the bandwidth between both these literature values, disagreement between the measured *ADC*'s and literature values could result from incorrect temperature estimation, because the temperature inside the magnet is not exactly known. Further deviations could result from the use of a linear interpolation between literature values. A maximum difference of up to 4% between water *ADC*'s for the PFG directions of Table 2.1 is measured, which could lead to a maximum *FA* bias of 0.02.

As mentioned in Section 5.1.3, the measured slice thickness deviates 10.6% from the calculated thickness. Since the exact pulse shape determines the frequency contents of the pulse and thus the shape of the slice profile, this discrepancy in thickness is possibly due to the excitation pulse deviating from a block-shape. Due to a non-infinitesimal RF switching time, the pulse shape is slightly smoothed, resulting in a frequency characteristic deviating from a sinc-function. For this study, only the relative signal contribution of the side-lobes is relevant. A consequence of these side-lobes is an overestimation of the *ADC* and an underestimation of the anisotropy when measuring tissue samples, because part of the signal originates from free water, which has a high diffusion constant ($\sim 2\times10^{-9}$ m^2/s) and is isotropic, and the measured *ADC* and anisotropy are averaged over tissue and water contributions. The exact slice profile, and its deviation from a sinc-shape, are only of importance when calculating slice thickness according to Eq. 2.12.

The optic nerve *ADC* is found to be increased by 77% compared to the measurement on a 6.3 T scanner directly following excision, while an *FA* decrease of 49% is observed. These changes are presumably caused by cell damage resulting from prolonged storage in a freezer. The preferential diffusion direction is found to be parallel to the long axis of the nerve, which agrees with the fact that the optic nerve consists of highly organized longitudinal fiber bundles. The lower section shows a preferential diffusion direction perpendicular to the long axis, which is assumed to result from fiber damage due to excision.

As the setup is calibration and validation, it is now optimized for the investigation of ischemia induced diffusion changes through DTI measurements of rat hippocampal slices, of which first results are presented in Section 5.3.

5.3 Hippocampus measurement results

5.3.1 Continuity measurement

From fast *ADC* measurements immediately following flow discontinuation, it is concluded that to prevent flow artifacts from influencing the measurement, a five minute delay is to be taken into account before commencing a DTI measurement. During this delay, residual macroscopic flow within the perfusion chamber will have ceased.

The Apparent Diffusion Coefficient and Fractional Anisotropy of hippocampal slices perfused with normal, oxygen saturated, aCSF have been monitored for approximately 4.5 hours. In this measurement, four hippocampal slices were in the central part of the image. In each hippocampus, a Region Of Interest (ROI) is defined, keeping a clearance from the edge in order not to include aCSF (ROI 1 through 4). The time evolution of both *ADC* and *FA* during the continuity measurement is shown in Figure 5.10. From

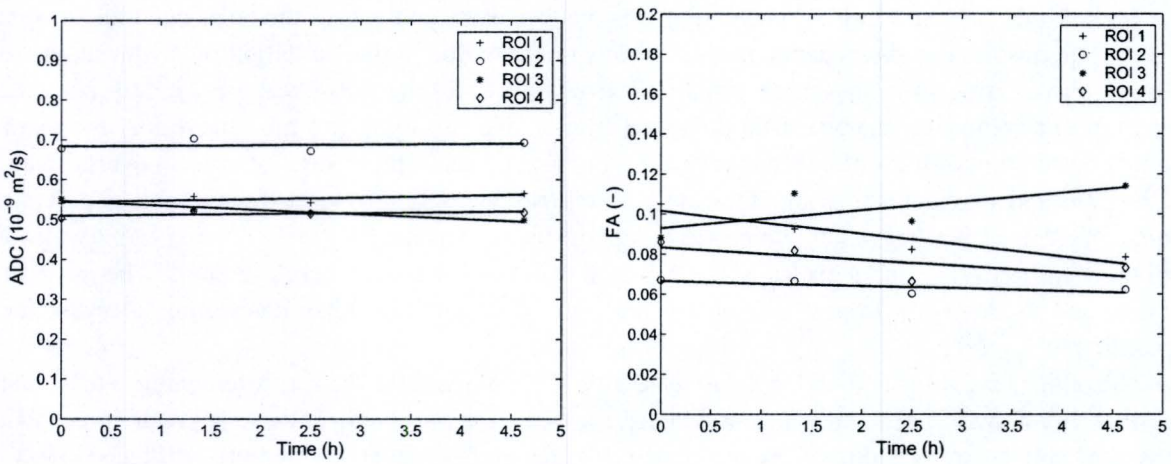

Figure 5.10: Time course of the Apparent Diffusion Coefficient and Fractional Anisotropy, with linear fits, for different hippocampal slices (ROI 1 through 4) during continuity measurement.

this figure, it can be seen that the *ADC* is virtually constant in time. Only ROI 3 shows a clear *ADC* decrease. Variations in *ADC* over the duration of the measurement are determined by fitting first-order polynomial functions, $y = ax + b$, to the data points of this figure. The resulting relative variations, measures for the constancy of the *ADC* expressed as $a/b \cdot 100\%$, are shown in Table 5.3.

The time evolution of the anisotropy is also shown in Figure 5.10. From this figure, it can be seen that, for ROI 2 and 4, the *FA* in nearly constant over the duration of the measurement. ROI 1 shows an *FA* decrease, while ROI 3 shows an increase. Variations over the duration of the measurement are determined analogous to *ADC* variations, and results are also shown in Table 5.3. The relative *ADC*

ROI	ΔADC	ΔFA
1	(0.8 ± 0.6)%	(-6 ± 2)%
2	(0.2 ± 0.7)%	(-2 ± 1)%
3	(-2.0 ± 0.4)%	(5 ± 3)%
4	(0.4 ± 0.5)%	(-4 ± 3)%

Table 5.3: Relative *ADC* and *FA* variation over the duration of the continuity measurement for different hippocampal slices (ROI 1 through 4).

increase over the duration of the measurement (4.5 hours) is below 1% for ROI 1, 2 and 4, while for

ROI 3 the *ADC* shows a decrease of 2%. Anisotropy decreases between 2% and 6% for ROI 1, 2 and 4, while ROI 3 shows an increase of 5%.

Following continuity measurements, staining is performed and CLSM images are acquired to determine cell viability. Figure 5.11 shows a typical CLSM image for one of the slices following the continuity measurement. From these images it can be seen that, although especially at the edges of the slice there

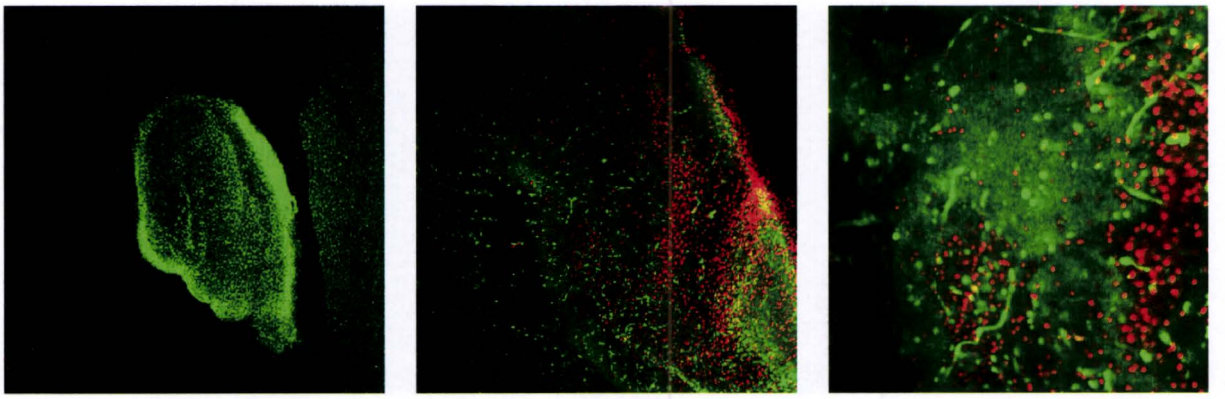

Figure 5.11: CLSM images of a hippocampal slice following continuity measurement. Images acquired using magnifications of 2.5x (left), 10x (center) and 20x (right).

is some cell damage resulting from slice procurement (indicated by red cells, shown most clearly in the image using a magnification of 10x), the majority of the cells have remained viable (indicated by green cells) during the continuity measurement. The image using a magnification of 20x also clearly shows viable axons (visible as green lines).

5.3.2 Osmolarity changes

Figure 5.12 shows typical *ADC* and *FA* maps for hippocampal slices subjected to osmotic perturbations, using colorcoding to obtain better visual distinctions. The typical hippocampal structure, as schemati-

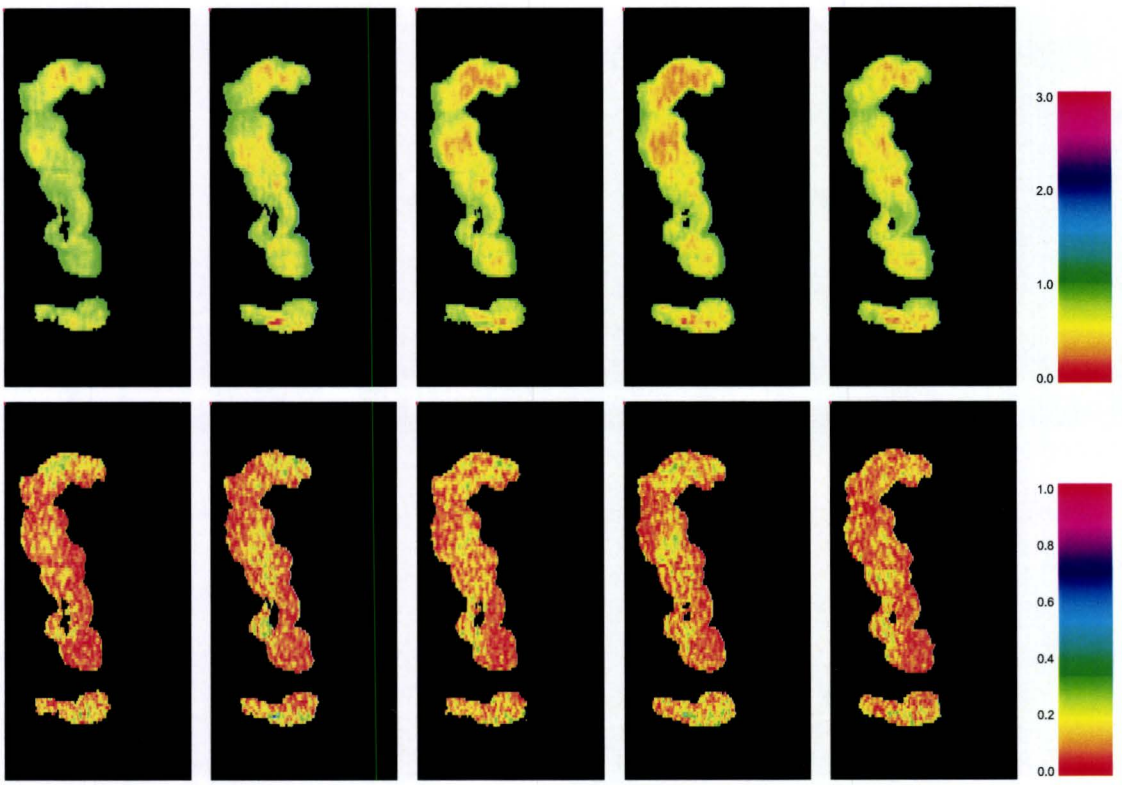

Figure 5.12: *ADC* (upper row) and *FA* (lower row) maps for hippocampal slices successively perfused with 10% hypertone, isotone, 10% hypotone, 20% hypotone and 30% hypotone aCSF.

cally shown in Figure 3.5 and imaged in Figure 5.9, is not recognizable. As the slices are positioned close together, it is difficult to distinguish individual slices. From Figure 5.12, an *ADC* increases can be seen when perfusing with hypertone aCSF. Images for perfusion with hypotone aCSF show a decreased *ADC* for up to 20% hypotone aCSF. The *ADC* rapidly increases when perfusing with 30% hypotone aCSF. Changes in *FA* are less pronounced. An increase is visible for up to 20% hypotone aCSF, while perfusion with 30% hypotone aCSF results in a clear *FA* decrease.

Analogous to the measurement described in Figure 5.12, additional measurements determining changes in *ADC* and *FA* as function of the osmolarity have been conducted. These are summarized in Figure 5.13, showing the *ADC* and *FA* as function of the relative osmolarity for different slices and different measurements. In this figure, the measurement described in Figure 5.12 is presented in the center row. Because the structure cannot be recognized, it was chosen to evaluate the central parts (CA1) as ROI, as the largest changes are expected in this region [1]. In the first measurement, shown in the top graphs, hippocampal slices were successively perfused with isotone, 10% hypotone, 20% hypotone, isotone, 10% hypertone and 20% hypertone aCSF. Due to the replacement of perfusion fluid between 20% hypotone and isotone aCSF, a discontinuity in both *ADC* and *FA* graphs is present. The *ADC* shows an increase for perfusion with hypertone aCSF. For perfusion with hypotone aCSF, a clear decrease is visible. The anisotropy shows relatively little change for perfusion with hypertone aCSF, while showing an increase for hypotone aCSF. The second measurement, shown in the center graphs, has been discussed through Figure 5.12. In the third measurement, shown in the bottom graphs, slices were successively perfused with 10% hyper-

tone, isotone, 10% hypotone, 20% hypotone and 30% hypotone aCSF. The *ADC* shows a clear decrease for decreasing osmolarity up to 20% hypotone. Further decrease, to 30% hypotone, results in an *ADC* increase. The anisotropy shows an increase for decreasing osmolarity up to 10% hypotone, while showing a decrease for further decreases in osmolarity.

The average relative *ADC* and *FA* of the measurements discussed above was calculated, as shown in Figure 5.14. To prevent distortion of the average values, two measurement points (indicated in Figure 5.13) were omitted from the calculations. These points were questionable due to 'hotspots' in the ROI. The relative *ADC* shows a linear relationship with the osmolarity between 20% hypotone and 10% hypertone. Below 20% hypotone, a rise is visible. Above 10% hypertone, no significant change is observed. The anisotropy generally shows an inversely proportional relationship with the osmolarity between 20% hypotone and 10% hypertone, with the exception of measurement three, which shows a decrease below 10% hypotone. Below 20% hypotone, a decrease is visible for both measurement two and three. Above 10% hypertone, no significant change is observed.

Following osmotic perturbations, viability staining is performed and CLSM images are acquired. Slices have proven to be difficult to remove from the setup without additional cell damage. It is also unknown which CLSM image corresponds to which ROI. Figure 5.15 shows a CLSM image of a hippocampal slice that has been subjected to up to 30% hypotonic aCSF. From the image using a magnification of 2.5x, it is clear that the slice is folded. Over the complete hippocampal slice, cell necrosis is visible. The image using a magnification of 20x shows some viable axons, among necrotic neurons and glia cells.

Figure 5.16 shows a CLSM image of a hippocampal slice that has been subjected to up to 20% hypotonic aCSF. The overview image, with a magnification of 2.5x, shows few necrotic cells, although the edges of the slice show some cell damage due to slice procurement. Because a thick imaging slice is selected, boundaries are visible. From the 10x image, viable cells and axons can clearly be seen.

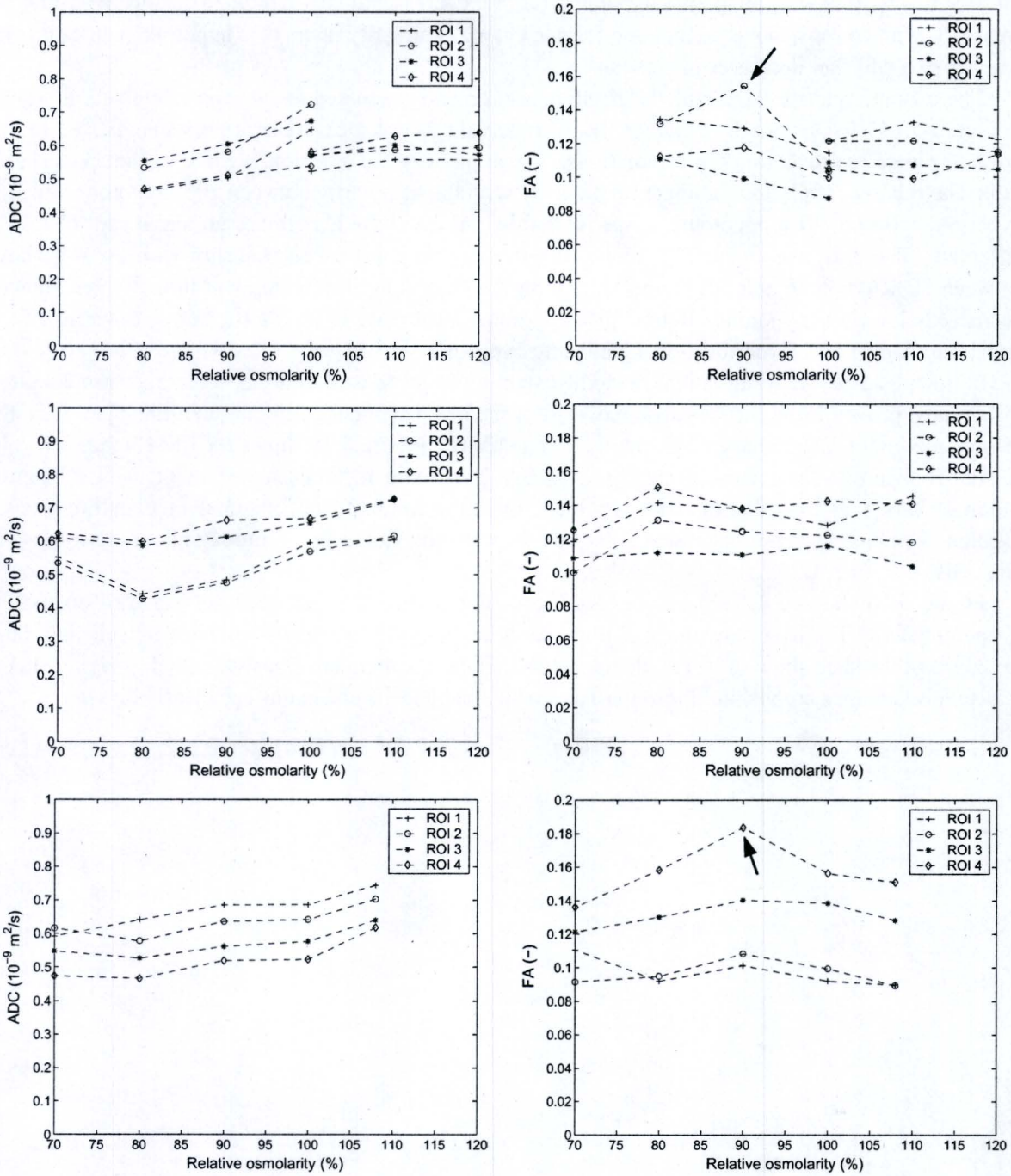

Figure 5.13: *ADC* (left column) and *FA* (right column) as function of the relative osmolarity for different hippocampal slices (ROI 1 through 4) and different measurements. During the first measurement (first row), hippocampal slices were successively perfused with isotone, 10% hypotone, 20% hypotone, isotone, 10% hypertone and 20% hypertone aCSF. Discontinuity results from switching perfusion fluids between 20% hypotone and isotone. During measurements two and three (second and third row), slices were successively perfused with 10% hypertone, isotone, 10% hypotone, 20% hypotone and 30% hypotone aCSF. The arrows in the top and bottom *FA* graphs indicate questionable points, omitted from further calculations.

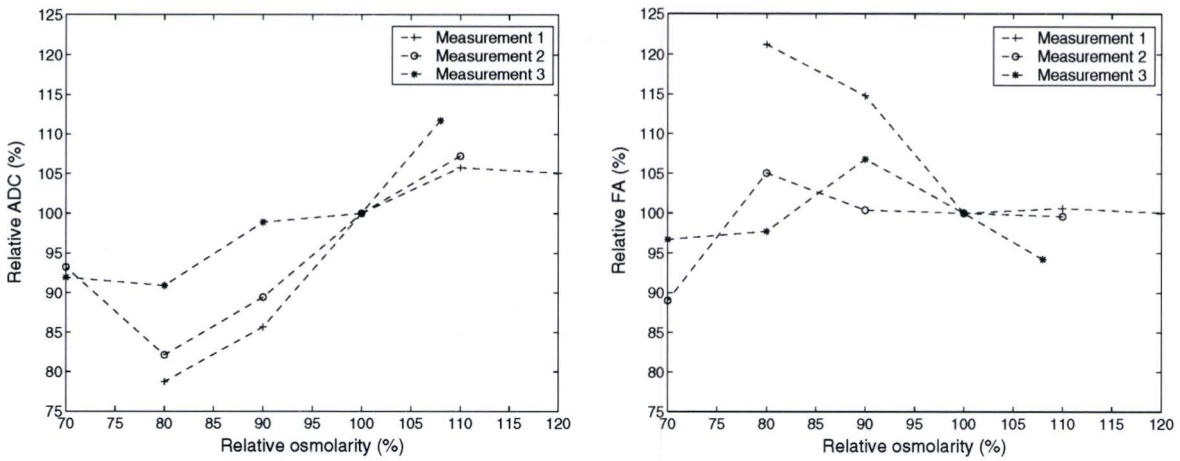

Figure 5.14: Average relative *ADC* and *FA* as function of the relative osmolarity for different measurements.

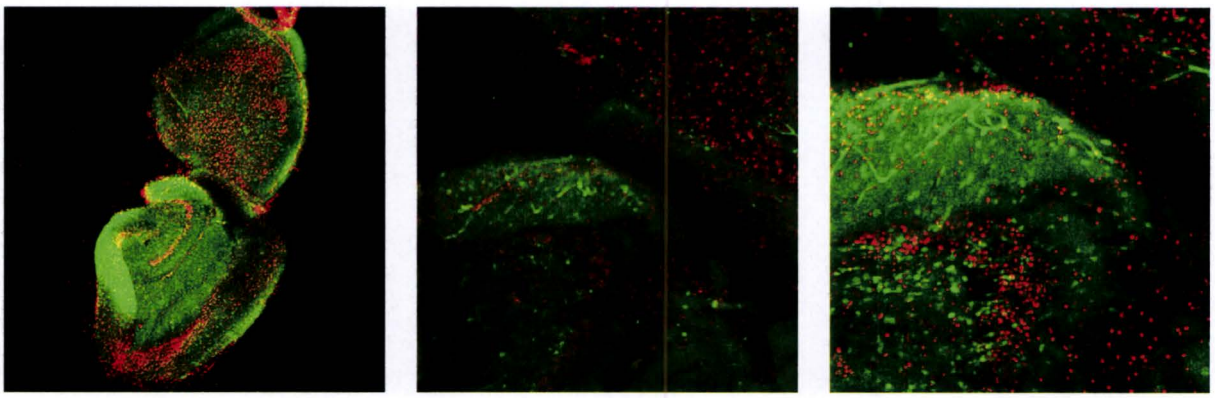

Figure 5.15: CLSM images of a hippocampal slice following osmotic perturbations of up to 30%. Images acquired using magnifications of 2.5x (left), 10x (center) and 20x (right).

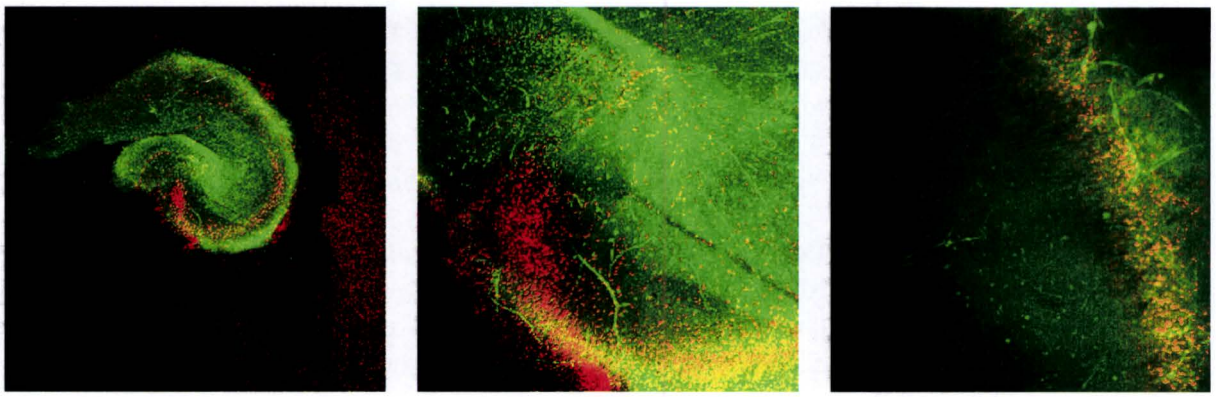

Figure 5.16: CLSM images of a hippocampal slice following osmotic perturbations of up to 20%. Images acquired using magnifications of 2.5x (left), 10x (center) and 20x (right).

5.3.3 Simulated ischemia

To establish the timescale of ischemia induced diffusion changes, the *ADC* is monitored for one PFG direction while subjecting hippocampal slices to glucose and oxygen deprivation. The results of this measurement can be seen in Figure 5.17. The *ADC* is seen to slowly decrease over the duration of the

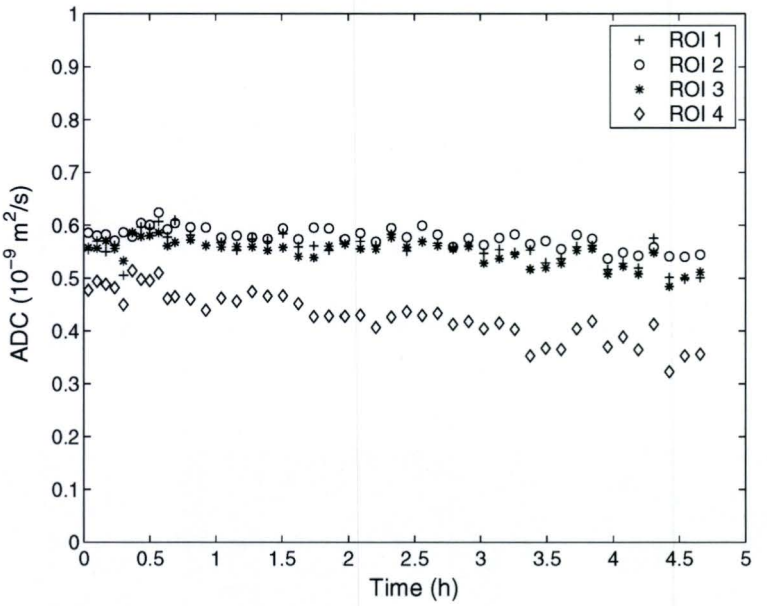

Figure 5.17: Time course of the Apparent Diffusion Coefficient for different hippocampal slices (ROI 1 through 4) under ischemic conditions, measured using only one PFG direction to obtain higher temporal resolution.

measurement. This decrease is more evident in ROI 4 than in the other ROI's. Because of the relatively large timescale of these changes, which occur over several hours, it is clear that the time resolution resulting from acquiring the complete diffusion tensor, which requires approximately 45 minutes, is sufficient to characterize ischemia induced diffusion changes.

From diffusion tensor measurements, the time course of both *ADC* and *FA* during ischemic conditions is determined, and is shown in Figure 5.18. For the first measurement, indicated in blue, the *ADC* decreases to about 50% of its initial value during the first ten hours of ischemia, and remains depressed during the following thirty-five hours of the measurement. The *ADC* step after 28 hours is caused by adjusting the RF-excitation frequency to prevent slice displacement. The second measurement, indicated in red, shows a similar, if somewhat slower, reduction in *ADC*, although ROI 3 and 4 show a reduced initial value compared to the first measurement. The sudden *ADC* rise in ROI 2 and 4 is caused by a displacement of the slices. Following this measurement, the pH of the perfusion fluid was found to have increased to pH = 8.

Figure 5.18 also shows the time course of *FA* during ischemic conditions. Within the first two to three hours, an increase in *FA* is observed for the first measurement, which is indicated in blue. Following the increase, the *FA* renormalizes within a time span of approximately five hours, and then remains constant during the remnant of the measurement. The second measurement, indicated in red, shows virtually no significant anisotropy change.

For several characteristic time points during simulated ischemia, Figure 5.19 displays *ADC* and *FA* maps. These time point are selected based on the time evolution of diffusion as shown in Figure 5.18, and show the baseline situation, maximum *FA*, a representative point in the middle of the *ADC* decrease and the stable end situation respectively. The *ADC* clearly shows a reduction from time point one to

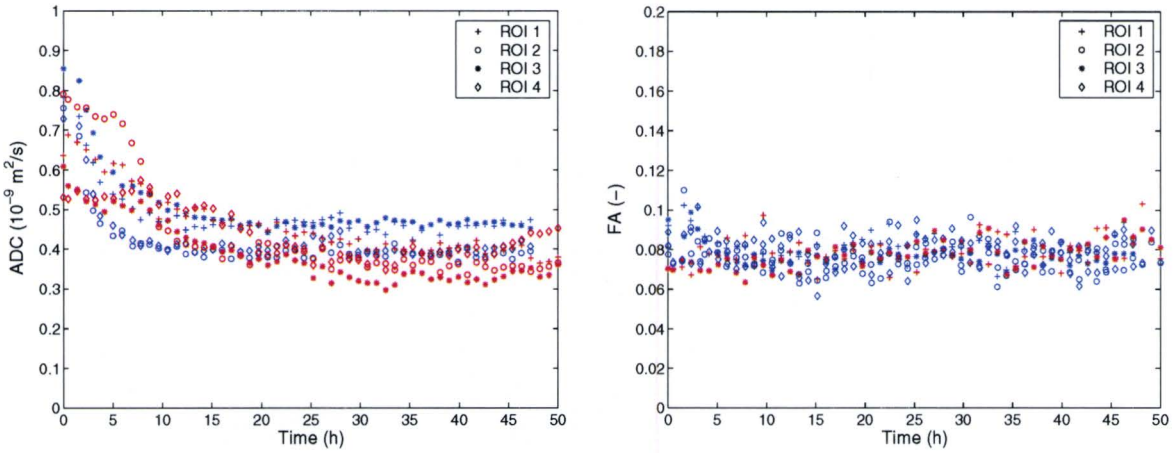

Figure 5.18: Time course of the Apparent Diffusion Coefficient (left) and Fractional Anisotropy (right) for different hippocampal slices (ROI 1 through 4) and different measurements (blue and red) under ischemic conditions.

four, for all the hippocampal slices. The *FA* shows a slight increase from time point one to two, while decreasing from time point two to four.

Following simulated ischemia, viability staining is performed and CLSM images are acquired. Figure 5.20 shows a typical CLSM image of an oxygen and glucose deprived hippocampal slice. These images are acquired following the fast *ADC* measurement, with the slices subjected to simulated ischemia for about 5 hours. Staining proved difficult due to tissue degradation. From the CLSM image with 2.5x magnification, it is clear that the slice, which is folded, contains many necrotic cells. The 20x image shows some viable axons, indicating the ischemia has not fully developed yet.

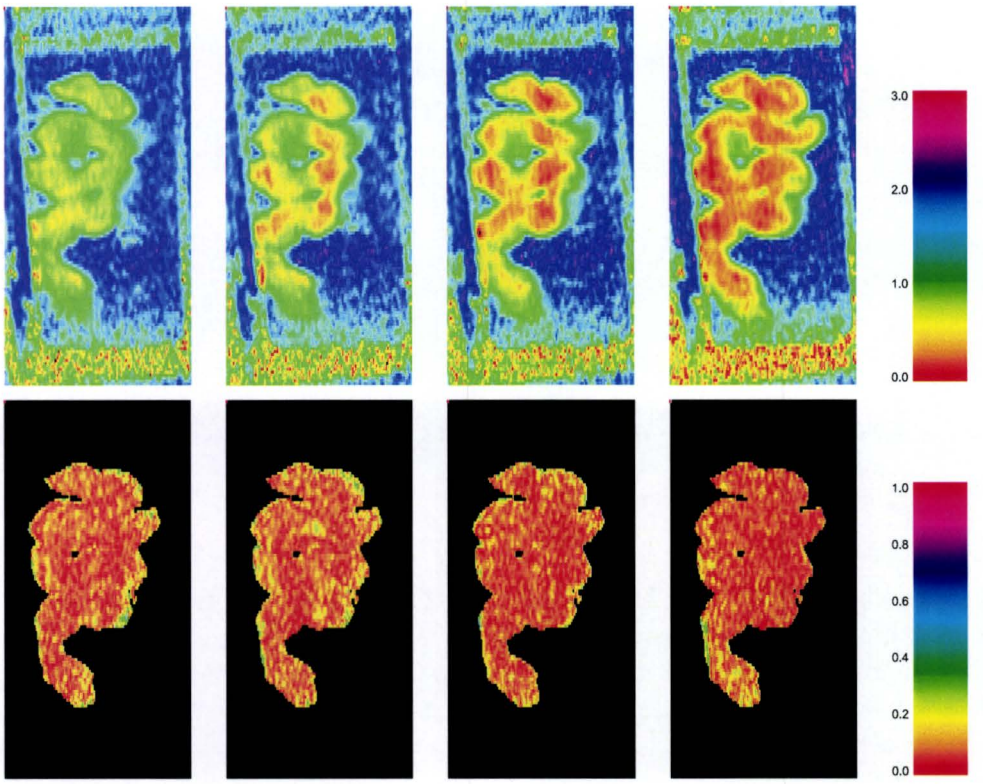

Figure 5.19: *ADC* (upper row) and *FA* (lower row) maps for characteristic time points (0, 2.3, 5.0 and 40.8 hours) during simulated ischemia. The *ADC* is given in units of 10^{-9} m^2/s.

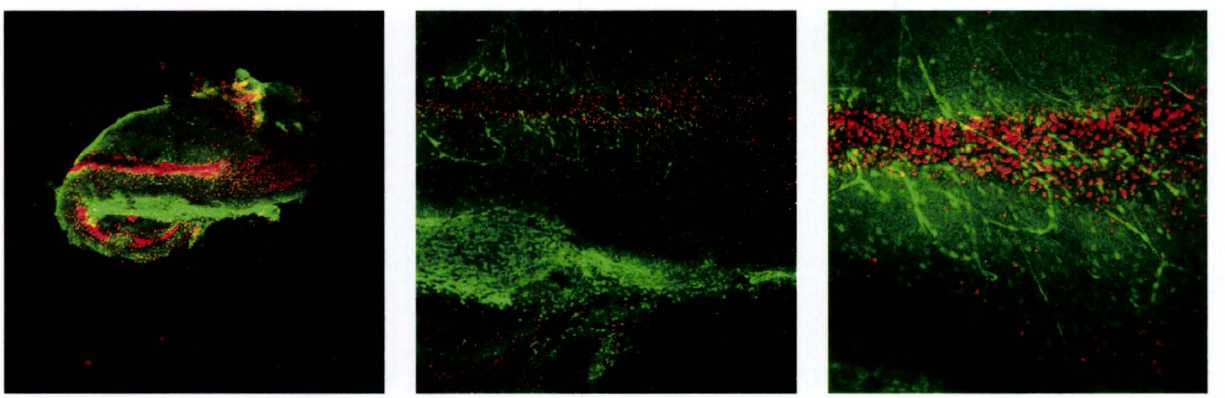

Figure 5.20: CLSM images of a hippocampal slice following oxygen and glucose deprivation. Images acquired using magnifications of 2.5x (left), 10x (center) and 20x (right).

5.3.4 Complete hippocampus

To visualize structure in rat pup hippocampi, and the presence of longitudinal components of fibers, which are lost during slice procurement, diffusion tensors of complete hippocampi are acquired. Figure 5.21 displays the *ADC*, the *FA* and a Color Code map of the non-fixated hippocampus. The *ADC*

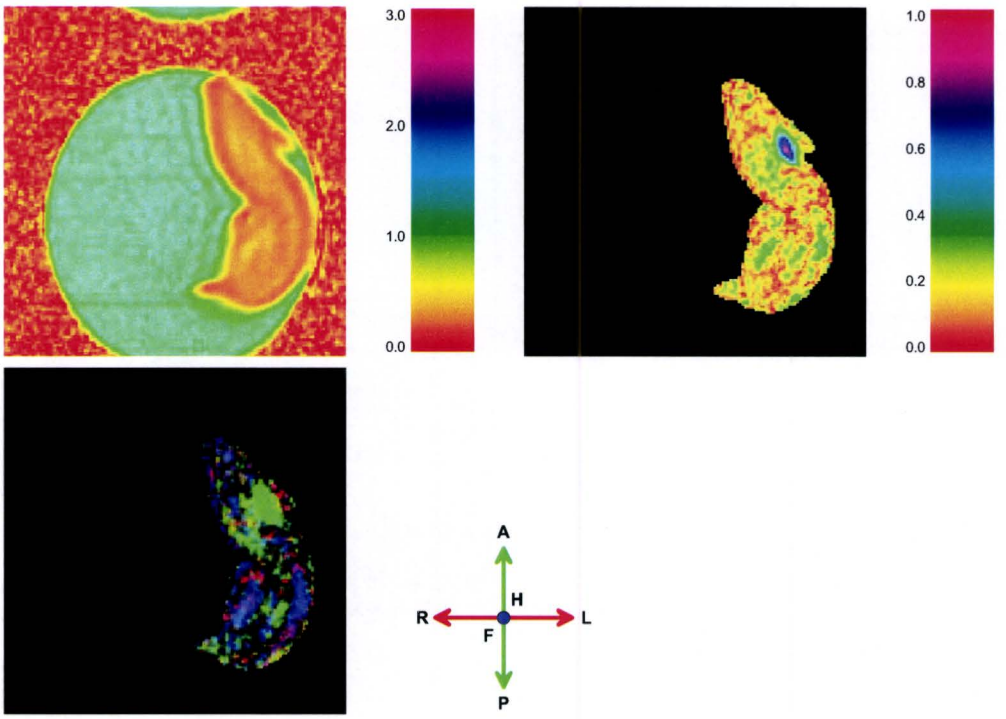

Figure 5.21: MR images of a non-fixated complete hippocampus, showing Apparent Diffusion Coefficient (top left), Fractional Anisotropy (top right) and Color Code (bottom left) of a transverse slice. The *ADC* is given in units of 10^{-9} m^2/s. Color Code image shows the directional preference of diffusion.

image shows a transverse slice through the hippocampus, which is located inside a tube containing water. The water signal is partially folded back, as can be seen at the top of the image. The image also shows some ghosting around the hippocampus, which is caused by the TSE sequence. The difference between gray matter and white matter, as shown in Figure 3.5, is visible in this image, as the gray matter regions show somewhat higher diffusion.The *FA* image shows a region of elevated anisotropy ($FA \approx 0.8$), which is most likely an artifact. This supposed artifact also appears in the color code map.From the color code image, the subiculum can be identified as a band with anterior-posterior diffusion preference, indicated by the green region in the right side of the image. It can also be seen that, within the hippocampus, diffusion is partly directed along the septotemporal axis, as indicated by the blue areas.

Figure 5.22 displays the *ADC*, the *FA* and a Color Code map of the formaldehyde fixated complete hippocampus. The *ADC* is decreased compared to the non-fixated hippocampus of Figure 5.21. Preferential diffusion directions are globally in agreement with Figure 5.21. Dissimilarities are partly caused by a different sample orientation, resulting in the switching of red and green colors. The subiculum is indicated by the red region in the upper side of the image. Diffusion is partly directed along the septotemporal axis, as indicated by the blue areas.

From both Figure 5.21 and Figure 5.22, it can be seen that hippocampal slices of rat pups show less structure compared to adult rats, as shown in Figure 5.9.

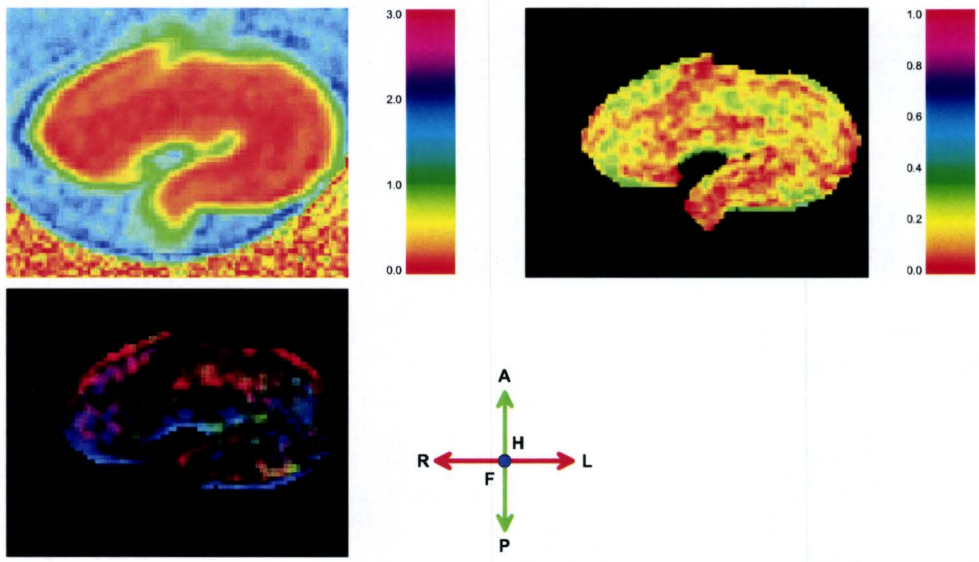

Figure 5.22: MR images of a fixated complete hippocampus, showing Apparent Diffusion Coefficient (top left), Fractional Anisotropy (top right) and Color Code (bottom left) of a transverse slice. The *ADC* is given in units of 10^{-9} m^2/s. Color Code image shows the directional preference of diffusion. Note that Color Code image differs from Figure 5.21. This is partly due to a different sample orientation.

5.4 Hippocampus measurement discussion

The imaging of rat pup hippocampal slices (with a diameter of 1-2 mm) was proven possible. The in-plane resolution of the obtained images is 141 μm, which results from a compromise between spatial and temporal resolution based on viability concerns. Although hippocampal slices of adult rats have been imaged before [28], the imaging of rat pup hippocampal slices, which are smaller and not fully developed (resulting in lower contrast and anisotropy), is novel.

As the slices imaged in this study are positioned close together, it is difficult to recognize individual slices. However, by always positioning the slices with the CA3 region towards the center, and by taking a picture of the slices before the perfusion chamber is placed inside the magnet, it is possible to distinguish slices.

In the *ADC* images, hippocampal structure, as schematically shown in Figure 3.5 and imaged in Figure 5.9, is not recognizable. This partly results from the use of young rats, which have a less developed brain compared to adult rats, as mentioned in 3.3. Since measurements are to be completed within approximately 45 minutes in order to resume perfusion and maintain cell viability, the resolution of these measurements is limited. This could also result in structure being less visible.

Cell swelling, resulting from osmotic perturbations, clearly induces changes in *ADC*. Decreasing the osmotic value of the perfusion fluid up to 20% results in a maximum *ADC* decrease of approximately 20%. Further osmolarity decreases result in an increase in *ADC*. Increasing the osmolarity by 10% leads to an increase in *ADC*. Anisotropy changes are less pronounced. The *FA* generally increases for osmolarity decreases up to 20%, while decreasing for further osmolarity decreases. Perfusion fluid osmolarity increases up to 10% lead to a decrease in *FA*.

The fact that hypertone aCSF has less effect on the *ADC* compared to hypotone aCSF could possibly be explained by the Donnan effect. Figure 5.23 shows the pressure response of a hydro gel as function of the osmotic value of the bathing solution [40]. For the material characterized in Figure 5.23, the pressure

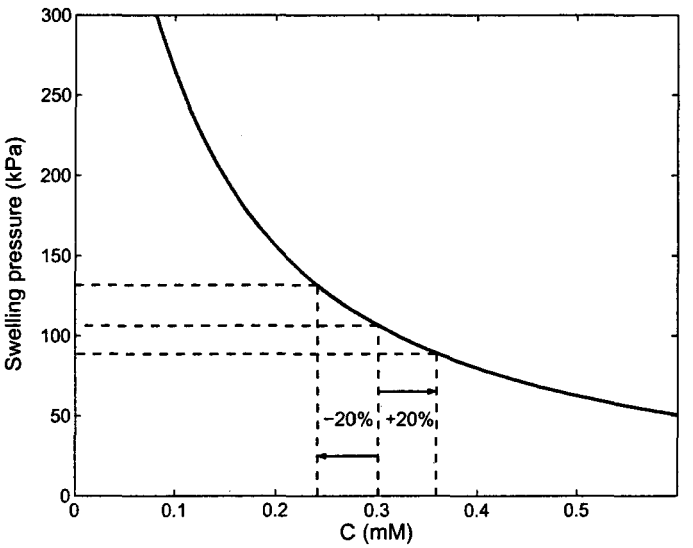

Figure 5.23: Pressure response of a hydro gel, as predicted by the Donnan effect, as function of the NaCl concentration of the bathing solution [40].

rise resulting from a 20% decrease in NaCl concentration is 18.4%, while the pressure decreases 12.7% when the NaCl concentration is increased by 20%. Viable cells are expected to yield similar pressure responses, but possible effects of active transport mechanisms complicate interpretation.

The *ADC* rise following perfusion with 30% hypotone aCSF is assumed to be caused by cell damage due to abnormal cell swelling. The degradation of restrictive barriers decreases tortuosity, hereby increasing the *ADC*. Loss of ordered structures also leads to a decrease in *FA*, as observed. This notion is corroborated by CLSM images, showing cell damage following perfusion with 30% hypotone aCSF.

Oxygen and glucose deprivation results in *ADC* changes on a time scale of several hours. Both the size and the timescale of these changes agree with changes observed in clinical studies, as depicted in Figure 3.3. The *ADC* decreases to approximately 50% over a period of ten hours. Since cell swelling only leads to a maximum *ADC* decreases of approximately 20%, this is not sufficient to explain ischemia induced changes. This implies that, in addition to the tortuosity theory and redistribution theory, which are related to cell volume as mentioned Section 3.2.2, other mechanisms are also responsible for diffusion changes.

Ischemia induced anisotropy changes are visible, but again less pronounced. Within the first two to three hours, an increase in *FA* is observed. Following the increase, the *FA* renormalizes within a time span of approximately five hours, and then remains constant during the remnant of the measurement. These changes are less evident than the *ADC* changes, and interpretation requires follow-up studies.

Of the ischemia measurements shown in Figure 5.18, the second measurement (depicted in red) shows a lower initial value for the *ADC*, and no significant *FA* change. This is possibly due to cell damage resulting from an incorrect pH of the perfusion fluid.

Measurements of complete hippocampi have visualized fiber structure, and indicate fibers parallel to the septotemporal axis. These longitudinal fiber structures will be lost during slice procurement. Due to this loss, slices will differ from in vivo tissue, which possibly influences the ischemic processes [8]. Differences in *ADC*, as measured between non-fixated and fixated hippocampi, are expected to be due to the formaldehyde fixation [37].

Limitations

In evaluating the results obtained, several limitations are to be taken into account. These will be discussed below.

Since this study relies on data obtained from an in vitro model, and these models differ from in vivo tissue, as described in Section 3.3, results may not directly translate to in vivo situations [8].

As mentioned in the discussion of the calibration measurements, the signal contribution of the sidelobes results in an overestimation of the *ADC*. The size of this overestimation depends on the relative contribution of free water to the signal, which changes as function of sample thickness, as indicated in Figure 5.24. This could account for part of the observed *ADC* change when osmotically perturbing hippocampal slices. When cell swelling occurs, the relative water contribution will decrease, resulting in a decrease in the measured average *ADC*. Cell shrinkage has the opposite effect. During isotone conditions, water contribution to the selected slice for a sample thickness of 500 μm is calculated to be 30.4%, based on geometric considerations, on the slice profile as measured and on the slice selection settings. This is maximum contribution, and the actual value is estimated to be lower, as will be discussed later. A volume increase of 20% would reduce the water contribution to 21.6%. Assuming *ADC*'s of 2.0×10^{-9} m^2/s for water and 0.7×10^{-9} m^2/s for tissue (a representative average value for WM and GM of rats [41, 42, 43]), the maximum influence of this effect on the *ADC* in case of cell swelling is a reduction of 10.5%. Since *ADC* reductions of up to 20% are observed, this effect is not sufficient to completely explain these changes, and the measurements therefore at least partially reflect actual changes in tissue *ADC* as function of osmolarity.

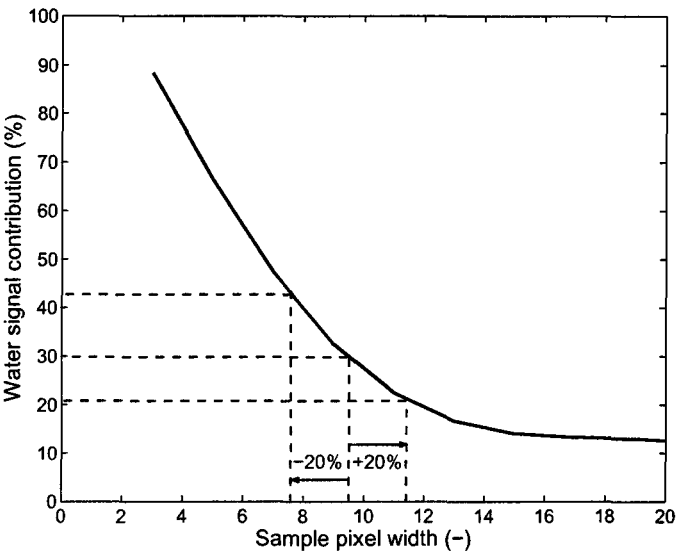

Figure 5.24: Relative signal contribution from water as function of sample thickness (denoted in pixels). Dashed lines indicate normal thickness and thickness resulting from 20% (osmotically driven) sample swelling or shrinkage.

It is assumed that the actual influence of aforementioned effect is less than 10.5%, because the observed tissue *ADC* is relatively low compared to values expected for a water contribution of 30%, and the actual tissue *ADC* is not expected to be severely decreased due to ischemia, as corroborated by CLSM images. The diffusion coefficient in the hippocampus has been measured to be 1.27×10^{-9} m^2/s (ADC_{fast}), using a bi-exponential fit to the signal attenuation as function of diffusion weighting [28]. Since this study measured a fast and slow diffusing component, measurements are not directly comparable.

If the actual diffusion coefficient is assumed to be 0.7×10^{-9} m^2/s, as in the calculation above, the measured *ADC* resulting from a water contribution would be 1.1×10^{-9} m^2/s. Since the effective *ADC* measured in this study is lower, and the actual tissue *ADC* is not expected to be severely decreased due to ischemia, it is therefore assumed that the water contribution is less than 30%.

Other studies have, through mono-exponential analysis of attenuation with b_{max} = 1169 s/mm^2, determined the *ADC* to be 0.45×10^{-9} m^2/s [44]. If this value is assumed to be representative, this would indicate a water contribution of approximately 16% in the baseline situation.

Above mentioned considerations indicate a water contribution lower than 30%, reducing the influence of changes in this contribution. Furthermore, slices are fixed between two nylon meshes, possibly limiting sample expansion in the slice selection direction and resulting changes in water contribution.

Due to the relatively low resolution required by time considerations, partial volume effects in the image may influence measurements. Voxels can contain white matter as well as gray matter, and since diffusion changes are generally greater in WM compared to GM [10], these changes may be partially obscured. To quantify the changes in diffusion, large ROI's, containing virtually the complete hippocampal slice, are selected. These regions are inhomogeneous and, like partial volume effects, this selection may further obscure changes in diffusion.

Since the duration of diffusion measurements following osmotic perturbations is approximately seven to eight hours, and ischemia induced diffusion changes extend over a relatively long time period (~10 h), the duration of the continuity measurement (Figure 5.10) is relatively short. To be able to make a better comparison between the time course of diffusion in normal, osmotically perturbed and ischemic tissue,

the continuity measurement should be sustained for approximately ten hours.

Anisotropy measurements are influenced by noise [45]. The signal to noise ratio of the images acquired in this study is approximately 30-40 for the diffusion weighted images, and 140 for the reference images. These values should be sufficient for anisotropy measured in this study to be originating from actual diffusion preferences, and not completely from noise [45].

Due to current losses within the superconducting coil, the main magnetic field decreases in time. As a result, the Larmor frequency decreases approximately 1 kHz every 12 hours, which is within the specifications of the magnet, necessitating frequency adjustments during sustained measurements. This adjustment results in measurement discontinuities, as shown in Figure 5.18.

The images resulting from viability staining are obtained using both Propidium Iodide and Calcein-AM, applied to tissue slices. As, in this group, there is only expertise concerning the effects of these dyes in cell suspensions, and the effects of Propidium Iodide in tissue, the obtained images have proven to be somewhat difficult to interpret. From a lack of PI-induced staining, it is assumed that viable cells are present.

Chapter 6

Conclusions

In this study, a setup has been developed to investigate ischemia induced diffusion changes by means of Diffusion Tensor Imaging of rat hippocampal slices. This setup consists of an MR system, with accompanying scan sequence, and a perfusion system.

For the MR system, a new send and receive coil was developed, as was a gradient rise time control box. The scan sequence implemented and used in this study is a Turbo Spin Echo Pulsed Field Gradient sequence. Calibrations and validations of the setup were performed. The perfusion system, developed to maintain slice viability, works although the pH of the aCSF sometimes changes over the duration of the measurement, possibly leading to cell damage. Slice viability is examined through fluorescence staining and subsequent acquisition of CLSM images. These images are difficult to interpret due to lack of expertise.

The setup yields realistic values for both *ADC* and *FA*, although due to the specific shape of the slice selection profile, the *ADC* is overestimated and the *FA* is underestimated when measuring thin tissue samples. Without perfusion fluid perturbations, the *ADC* and *FA* of rat pup hippocampal slices were shown to remain constant for several hours.

Osmotic perturbations yield clear *ADC* changes. Decreasing the osmotic value of the perfusion fluid up to 20% results in an maximum *ADC* decrease of approximately 20%. Further osmolarity decreases results in cell damage, characterized by an increase in *ADC* and a decreased anisotropy. Increasing the osmolarity up to 10% leads to an increase in *ADC*. Anisotropy changes are less pronounced. The *FA* generally shows an increase for osmolarity decreases up to 20%, while decreasing for osmolarity increases up to 10%.

Ischemia is simulated through oxygen and glucose deprivation of the perfusion fluid. Both the amount and the timescale of the *ADC* changes following oxygen and glucose deprivation agree with *ADC* changes observed in clinical studies, as depicted in Figure 3.3. The *ADC* decreases to approximately 50% of the initial value over a period of ten hours. This decrease can not fully be explained by changes due to cell swelling, since these only lead to a maximum decrease of approximately 20%. The anisotropy shows an increase and subsequent renormalization within several hours. These changes are less evident than the *ADC* changes, and interpretation requires follow-up studies.

To investigate fiber structure in the rat pup hippocampus, and loss of structure due to slice procurement, complete hippocampi were imaged. From these measurements, the hippocampus was shown to contain regions of longitudinal fiber orientation, perpendicular to the slice direction. When slices are obtained, these fibers are damaged, which possibly influences ischemic processes.

As mentioned, the setup developed in this study yields realistic results, and the in vitro hippocampal slices seem to be a good model. Interpretation of some of the measurement results, however, requires follow-up studies.

Chapter 7

Recommendations

From the results of this study, it has been shown that specific aspects of the setup can influence measurement results. To further improve measurements, several modifications and improvements are required. Section 7.1 discusses several experimental setup improvements that will increase measurement accuracy. Section 7.2 gives recommendations for future measurements.

7.1 Experimental setup

To further improve the experimental setup and obtain more accurate measurement results, a series of modifications will be discussed in detail. These are:

1. NMR setup
    - increasing SNR
    - using sinc-shaped excitation pulses
    - using realtime RF-power adjustment
    - controlling gradient rise-times through the ASG
    - planning (selection of off-center slices and voxels)
    - incorporating automatic frequency adjustment
    - using outer volume suppression
2. Perfusion setup
    - continuously monitoring pH and pO_2
    - improving air bubble removement

Increasing SNR

Increasing the Signal to Noise Ratio increases the accuracy of *FA* measurements and could reduce measurement time. A method to accomplish this increase is by coil downsizing, which increases the fill factor F and, since SNR $\propto \sqrt{F}$, this increases the SNR. This can also be accomplished by using a cryo-coil, which reduces intrinsic temperature related receiver coil noise (SNR $\propto 1/\sqrt{T}$). A third way to increase the SNR is applying a multi-coil technique (e.g. quadrature coils or SENSE). Multi-coil techniques increase the SNR by simultaneously recording the MR signal though multiple coils and, because the recorded signal of the coils is correlated while noise is uncorrelated, noise can be averaged out, thus increasing the SNR. A possible way to implement a multi-coil technique is using quadrature coils. Here, two independent 90°-phase-shifted signals are obtained. These signals can be combined to produce a signal with a signal to noise ratio that is $\sqrt{2}$ times greater than the SNR of a single coil.

Sinc-shaped excitation pulses

Sinc-shaped excitation pulses allow for block shaped slice profiles, eliminating excessive water signal contribution to tissue *ADC* measurements. This improvement requires hardware and software modifications. A new send/receiver unit is required, with the possibility to adjust the RF-power in realtime. The new pulse shape also has to be incorporated in the software.

Realtime RF-power adjustment

Realtime RF-power adjustment allows altering the RF-power between pulses. With this modification, requiring a new send/receive unit as described earlier, it would be possible to use equals pulse durations for 90- and 180-degree pulses. With equal pulse durations, the frequency content of the pulses is the same, thus slice selection during the 90- and 180-degree pulses results in equal slice thicknesses and excitation of the same sample fragment for each pulse. This reduces unwanted signals resulting from pulse imperfections, resulting in a better defined signal source volume.

ASG controlled gradient rise-times

Controlling gradient rise-times through the analog signal generator (ASG) instead of the rise-time control box eliminates gradient overshoots and oscillations, giving better defined gradient lobes and thereby increasing measurement accuracy. This modification requires changes in software. Because every point of the gradient shape has to be defined, enormous amounts of data are generated for complex pulse sequences.

Planning

Planning requires RF-sending and receiving with different frequencies, hereby selecting off-center slices and/or voxels, simplifying sample alignment. This could decrease sample preparation time and possibly increase alignment accuracy. It also enables single voxel measurements, reducing measurement time. When conducting single voxel measurements, it is necessary to be able to select a specific off-center voxel due to the inhomogeneous nature of the sample and the absence of an in-plane sample movement mechanism.

Frequency adjustment

Automatic frequency adjustment compensates for changes in Larmor frequency, which decreases approximately 1 kHz every hour. The change in resonance frequency, resulting in the selection of incorrect slices and loss of signal, is caused by a decreasing main magnetic field, and is within fabrication specifications. A possible complication of using frequency adjustment is the tuning of the receive coil. Because the coil has a limited bandwidth, large changes in the resonance frequency result in a signal decrease.

Outer volume suppression

Outer volume suppression enables the selection of a smaller Field of View, resulting in a higher resolution, without resulting in excessive folding back. This is accomplished by adding pre-pulses to the sequence. These pre-pulses crush outer volume magnetization.

Monitoring pH and pO_2

Since during measurements changes in pH were detected, continuously monitoring pH and pO_2 would facilitate maintaining proper perfusion fluid specifications.

Air bubble removement

Because air bubbles inside the perfusion chamber influence the measured signal, these should be prevented. A possible solution would be to include an expansion chamber, collecting all air bubbles. From this chamber, the bubbles can then be removed.

7.2 Measurements

An important measurement to perform once more is a continuity measurement, since the duration of the measurement was only 4.5 hours. The measurement should be performed for a prolonged period, eight to ten hours minimum, and care should be taken to avoid slice procurement related cell damage and to maintain proper perfusion fluid specifications.

Since hippocampal slices have proven to be difficult to remove from the setup following measurements, viability staining could possibly be facilitated by using control slices. These slices are not fixed on a mesh and located within the magnet, but are subjected to the same perfusion fluid perturbations.

Since the rats used in this study are between eight and twelve days old, the brain axon myelinization is not yet completed. This results in a lower anisotropy compared to adult rats. Due to this, anisotropy is difficult to measure, and changes therein are difficult to interpret. Measuring hippocampal slices of adult rats, which are less suited as neonatal ischemia models, but offer higher anisotropy, could facilitate investigating ischemia induced anisotropy changes.

The slice procurement procedure as used in this study results in cell damage. To reduce this damage, tissue cultures could be used. Cultures are grown on a medium, and necrotic cells are removed. The disadvantage of using cell cultures is that the medium limits the possibility to influence the extracellular environment during the measurements.

Through the use of contrast agents (e.g. Gd-DTPA or iron oxides), it is possible to exclude the signal contribution of the ECS from the measurements. This would enable investigation of intracellular diffusion changes.

By acquiring T_2 maps (multi-echo or CPMG), relative contributions of compartments with different relaxation and diffusion properties can be identified and monitored. A beginning has already been made by incorporating a multi-echo T_2-mapping mode into the pulse sequence developed in this study.

Another interesting new measurement would be the investigation of reperfusion injury, since the mechanisms underlying this damage are not exactly known, as briefly discussed in Section 3.2. These measurements could perhaps be performed in combination with histology. By subjecting slices to oxygen-glucose deprivation for a short period and then resuming perfusion with normal aCSF, reperfusion can be simulated.

Bibliography

[1] C. M. P. C. D. Peeters-Scholte. *Neuroprotective strategies following perinatal hypoxia-ischemia.* PhD thesis, Utrecht University, Fac. of Medicine, 2002.

[2] W. B. Veldhuis. *Neuroprotection Against Exctitoxicity and Inflammation in Acute Ischemic Stroke.* PhD thesis, Utrecht University, Fac. of Medicine, 2003.

[3] P. S. Huppi and P. D. Barnes. Magnetic resonance techniques in the evaluation of the newborn brain. *Clin. Perinatol.*, 24(3):693–723, 1997.

[4] T. M. Shepherd, III E. D. Wirth, P. E. Thelwall, H. X. Chen, S. N. Roper, and S. J. Blackband. Water diffusion measurements in perfused human hippocampal slices undergoing tonicity changes. *Magn Reson. Med.*, 49(5):856–863, 2003.

[5] E. O. Stejskal and J. E. Tanner. Spin diffusion measurements: spin echoes in the presence of a time-dependent field gradient. *J. Chem. Phys.*, 42:288–292, 1965.

[6] D. K. Jones, M. A. Horsfield, and A. Simmons. Optimal strategies for measuring diffusion in anisotropic systems by magnetic resonance imaging. *Magn Reson. Med.*, 42(3):515–525, 1999.

[7] M. T. Vlaardingerbroek and J. A. den Boer. *Magnetic Resonance Imaging, Theory and Practice.* Springer-Verlag, Berlin, 3rd edition, 2002.

[8] P. Lipton. Ischemic cell death in brain neurons. *Physiol Rev.*, 79(4):1431–1568, 1999.

[9] R. M. Dijkhuizen. *Magnetic Resonance Imaging and Spectroscopy in Experimental Cerebral Ischemia.* PhD thesis, Utrecht University, Fac. of Medicine, 1998.

[10] C. H. Sotak. The role of diffusion tensor imaging in the evaluation of ischemic brain injury - a review. *NMR Biomed.*, 15(7-8):561–569, 2002.

[11] Q. Yang, B. M. Tress, P. A. Barber, P. M. Desmond, D. G. Darby, R. P. Gerraty, T. Li, and S. M. Davis. Serial study of apparent diffusion coefficient and anisotropy in patients with acute stroke. *Stroke*, 30(11):2382–2390, 1999.

[12] F. Zelaya, N. Flood, J. B. Chalk, D. Wang, D. M. Doddrell, W. Strugnell, M. Benson, L. Ostergaard, J. Semple, and S. Eagle. An evaluation of the time dependence of the anisotropy of the water diffusion tensor in acute human ischemia. *Magn Reson. Imaging*, 17(3):331–348, 1999.

[13] R. A. Carano, F. Li, K. Irie, K. G. Helmer, M. D. Silva, M. Fisher, and C. H. Sotak. Multispectral analysis of the temporal evolution of cerebral ischemia in the rat brain. *J. Magn Reson. Imaging*, 12(6):842–858, 2000.

[14] A. E. Baird and S. Warach. Magnetic resonance imaging of acute stroke. *J. Cereb. Blood Flow Metab*, 18(6):583–609, 1998.

[15] E. Sykova, J. Svoboda, J. Polak, and A. Chvatal. Extracellular volume fraction and diffusion characteristics during progressive ischemia and terminal anoxia in the spinal cord of the rat. *J. Cereb. Blood Flow Metab*, 14(2):301–311, 1994.

[16] A. van der Toorn. *Localized in vivo NMR spectroscopy. Applications to experimental brain ischemia.* PhD thesis, Utrecht University, Fac. of Chemistry, 1995.

[17] A. Szafer, J. Zhong, and J. C. Gore. Theoretical model for water diffusion in tissues. *Magn Reson. Med.*, 33(5):697–712, 1995.

[18] D. Krizaj, M. E. Rice, R. A. Wardle, and C. Nicholson. Water compartmentalization and extracellular tortuosity after osmotic changes in cerebellum of trachemys scripta. *J. Physiol*, 492 (Pt 3):887–896, 1996.

[19] T. Q. Duong, J. J. Ackerman, H. S. Ying, and J. J. Neil. Evaluation of extra- and intracellular apparent diffusion in normal and globally ischemic rat brain via 19f nmr. *Magn Reson. Med.*, 40(1):1–13, 1998.

[20] T. Niendorf, R. M. Dijkhuizen, D. G. Norris, Campagne M. van Lookeren, and K. Nicolay. Biexponential diffusion attenuation in various states of brain tissue: implications for diffusion-weighted imaging. *Magn Reson. Med.*, 36(6):847–857, 1996.

[21] J. V. Sehy, J. J. Ackerman, and J. J. Neil. Evidence that both fast and slow water adc components arise from intracellular space. *Magn Reson. Med.*, 48(5):765–770, 2002.

[22] T. Q. Duong, J. V. Sehy, D. A. Yablonskiy, B. J. Snider, J. J. Ackerman, and J. J. Neil. Extracellular apparent diffusion in rat brain. *Magn Reson. Med.*, 45(5):801–810, 2001.

[23] J. V. Sehy, J. J. Ackerman, and J. J. Neil. Apparent diffusion of water, ions, and small molecules in the xenopus oocyte is consistent with brownian displacement. *Magn Reson. Med.*, 48(1):42–51, 2002.

[24] M. Hoehn, K. Nicolay, C. Franke, and Sanden B. van der. Application of magnetic resonance to animal models of cerebral ischemia. *J. Magn Reson. Imaging*, 14(5):491–509, 2001.

[25] P. G. Aitken, G. R. Breese, F. F. Dudek, F. Edwards, M. T. Espanol, P. M. Larkman, P. Lipton, G. C. Newman, Jr. T. S. Nowak, K. L. Panizzon, and . Preparative methods for brain slices: a discussion. *J. Neurosci. Methods*, 59(1):139–149, 1995.

[26] S. J. Blackband, J. D. Bui, D. L. Buckley, T. Zelles, H. D. Plant, B. A. Inglis, and M. I. Phillips. Mr microscopy of perfused brain slices. *Magn Reson. Med.*, 38(6):1012–1015, 1997.

[27] D. L. Buckley, J. D. Bui, M. I. Phillips, and S. J. Blackband. Mri measurement of cell volume fraction in the perfused rat hippocampal slice. *Magn Reson. Med.*, 42(3):603–607, 1999.

[28] T. M. Shepherd, S. J. Blackband, and III E. D. Wirth. Simultaneous diffusion mri measurements from multiple perfused rat hippocampal slices. *Magn Reson. Med.*, 48(3):565–569, 2002.

[29] T. M. Shepherd, P. E. Thelwall, S. J. Blackband, B. R. Pike, R. L. Hayes, and E. D. Wirth III. Diffusion magnetic resonance imaging study of a rat hippocampal slice model for acute brain injury. *J. Cereb. Blood Flow Metab*, 23(12):1461–1470, 2003.

[30] G. Paxinos. *The Rat Nervous System.* Academic Press, San Diego CA., 2nd edition, 1995.

[31] A. C. Guyton and J. E. Hall. *Textbook of Medical Physiology*. W. B. Saunders Company, Philadelphia PA., 9th edition, 1996.

[32] E. B. Isaacs, A. Lucas, W. K. Chong, S. J. Wood, C. L. Johnson, C. Marshall, F. Vargha-Khadem, and D. G. Gadian. Hippocampal volume and everyday memory in children of very low birth weight. *Pediatr. Res.*, 47(6):713–720, 2000.

[33] L. Rijniers. NMR Relaxation Measurements on H and Na in porous Media. Master's thesis, Eindhoven University of Technology, Dept. of Applied Physics, 2000.

[34] Doty. *Gradient Probe Clear Bore, User Manual DSI-772*. Doty Scientific, Inc., 1999.

[35] R. Monette, D. L. Small, G. Mealing, and P. Morley. A fluorescence confocal assay to assess neuronal viability in brain slices. *Brain Res. Brain Res. Protoc.*, 2(2):99–108, 1998.

[36] G. J. Stanisz, A. Szafer, G. A. Wright, and R. M. Henkelman. An analytical model of restricted diffusion in bovine optic nerve. *Magn Reson. Med.*, 37(1):103–111, 1997.

[37] S. W. Sun, J. J. Neil, and S. K. Song. Relative indices of water diffusion anisotropy are equivalent in live and formalin-fixed mouse brains. *Magn Reson. Med.*, 50(4):743–748, 2003.

[38] J. H. Simpson and H. Y. Carr. Diffusion and nuclear spin relaxation in water. *Phys. Rev.*, 111(5):1201–1202, 1958.

[39] R. Mills. Self-Diffusion in Normal and Heavy Water in the Range 1-45°*C*. *J. of Phys. Chem.*, 77:685–688, 1972.

[40] H. J. de Heus. *Verification of Mathematical Models Describing Soft Charge Hydrated Tissue Behaviour*. PhD thesis, Eindhoven University of Technology, 1994.

[41] M. D. Does, E. C. Parsons, and J. C. Gore. Oscillating gradient measurements of water diffusion in normal and globally ischemic rat brain. *Magn Reson. Med.*, 49(2):206–215, 2003.

[42] C. D. Kroenke, J. J. Ackerman, and J. J. Neil. Magnetic resonance measurement of tetramethylammonium diffusion in rat brain: Comparison of magnetic resonance and ionophoresis in vivo diffusion measurements. *Magn Reson. Med.*, 50(4):717–726, 2003.

[43] C. Meier, W. Dreher, and D. Leibfritz. Diffusion in compartmental systems. ii. diffusion-weighted measurements of rat brain tissue in vivo and postmortem at very large b-values. *Magn Reson. Med.*, 50(3):510–514, 2003.

[44] D. L. Buckley, J. D. Bui, M. I. Phillips, T. Zelles, B. A. Inglis, H. D. Plant, and S. J. Blackband. The effect of ouabain on water diffusion in the rat hippocampal slice measured by high resolution nmr imaging. *Magn Reson. Med.*, 41(1):137–142, 1999.

[45] P. J. Basser and S. Pajevic. Statistical artifacts in diffusion tensor mri (dt-mri) caused by background noise. *Magn Reson. Med.*, 44(1):41–50, 2000.

[46] T. W. Scheenen, D. van Dusschoten, P. A. de Jager, and H. Van As. Microscopic displacement imaging with pulsed field gradient turbo spin-echo nmr. *J. Magn Reson.*, 142(2):207–215, 2000.

[47] H. T. Edzes, D. van Dusschoten, and H. Van As. Quantitative t2 imaging of plant tissues by means of multi-echo mri microscopy. *Magn Reson. Imaging*, 16(2):185–196, 1998.

[48] A. P. Crawley and R. M. Henkelman. Errors in t2 estimation using multislice multiple-echo imaging. *Magn Reson. Med.*, 4(1):34–47, 1987.

Appendix A

TSE-PFG pulse sequence features

The pulse sequence implemented and used in this study is a Turbo Spin Echo Pulsed Field Gradient (TSE-PFG) sequence, with centric k-line order and slice selection around the 90 and/or 180 degree pulse. The sequence has the option to measure a Field of View with a 2:1 aspect ratio, by halving the number of phase encoding steps. The in-plane resolution remains isotropic.

Slice selection rephasing can be optimized by measuring the zeroth k-line repeatedly, while varying the rephasing length scaling factor. The optimal scaling factor yields maximum signal intensity.

Furthermore, the timing of the turbo sequence can be validated by switching off the phase encoding gradient and measuring the same k-line repeatedly. Each time, the echo should appear at the same position.

Pulsed Field gradients are used for diffusion weighting, and it is possible to measure a full DTI tensor at a specified number of b-values [46]. Diffusion time variation is also possible. To optimize signal intensities when measuring both diffusion weighted images and reference images, it is possible to prescribe a signal amplifier gain change, thus optimizing gain for both images separately.

It's also possible to measure T_2 maps, by means of multi-echo imaging. In this mode, multiple echoes are measured for each k-line, and an image is made for each echo. By evaluating the signal decrease of each pixel for consecutive echoes, it's possible to determine the T_2 value [47]. To eliminate unwanted echoes causing errors in T_2 estimation, spoiler gradients are used [48].

Appendix B

Coil characteristics

Figure B.1 displays the frequency characteristics of the RF excitation and detection coil. From this

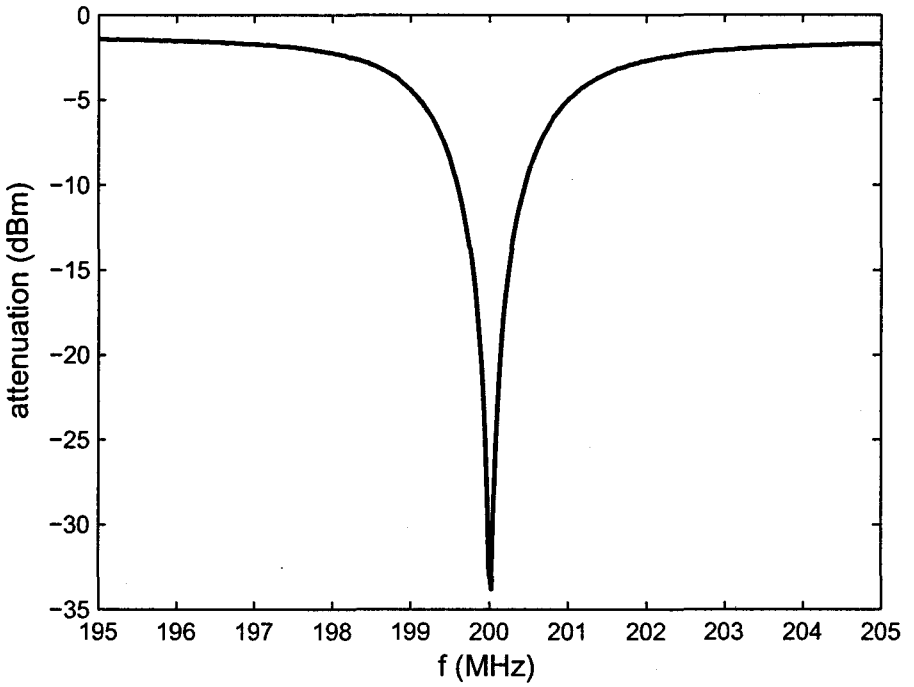

Figure B.1: Frequency characteristics of the RF coil.

figure, it can be seen that the resonance frequency of the coil is 200 MHz, corresponding to the Larmor frequency at a magnetic field strength of 4.7 T.

Appendix C

Literature water diffusion coefficients

Figure C.1 [38, 39] displays the diffusion coefficient of water as function of the temperature.

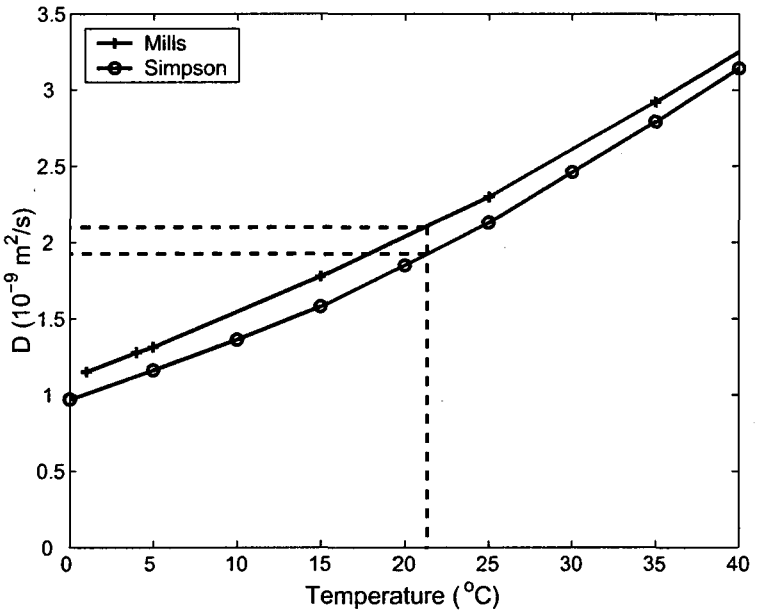

Figure C.1: Water diffusion coefficient as function of temperature, as found by Mills [39] (+) and Simpson *et al* [38] (o). Dashed lines indicate the diffusion coefficients at a water temperature of 21.3°*C*.

Acknowledgements

I would like to thank everyone who helped me during my graduation research and, without detracting from somebodies merits, would hereby like to thank some people in special:

First of all, I would like to thank my direct supervisor, Carola van Pul, for introducing me to the world of diffusion weighted imaging and ischemia, for the pleasant collaboration, for all the time spent reading and correcting this report, and for everything I forget to mention.

I would also like to thank the committee: Prof.dr.ir. P.F.F. Wijn, Prof.dr.ir. K. Kopinga, Prof.dr. K. Nicolaij, dr. R.A.H. Engeln, drs. J. Buijs and ir. C. van Pul.

Furthermore, I would like to thank Jaap Feijen, who truly has proven to be versatile and indispensable, whether in the workshop, behind the computer, or during theoretical discussions.

A special thanks to Jef Noijen, among others for continuously fixing our gradients (sometimes a frustrating job, but absolutely worthwhile in the end).

I would also like to thank Lourens Rijniers and Bart Erich, for their help with programming and with the 4.7T setup, Hans Dalderop, for his assistance with parts of the perfusion setup and with the ion chromatography, Jo Habets, for his help with the DEC protocol and the preparation of the animals, Edwin Heijman, for his help with Matlab and the ellipse fitting routine, Henk Huinink, for sharing his theories and points of view and Gustav Strijkers, for many helpful articles and discussions.

I would also like to thank the people at the workshop, for their help manufacturing our perfusion chamber (it appears that, contradictory to the saying, two times is a charm).

I would also like to thank Bas Clasquin, for showing me how to work with 'Eagle' and for his help with the fabrication of the gradient control box (we couldn't have done our measurements without it!).

I would also like to thank Peter Sodaar and Marjolein Vliem from the UMC, for their tissue preparation lessons and help with the staining protocols.

Not to forget, my fellow students, and in special Geralda van Tilborg and Bob Hamans, for their continuous help and support, whether it be with LaTeX, Matlab or through mental support. I would also like to thank all my other colleagues at MRL.

Last but not least, I would like to thank my family and friends for all their help and support, and in special my parents, for supporting me both mentally and through assistance during the final stage of this project.